iScience

Article

Investigations on full-Heusler alloys Mn_2TaAl and Mn_2WAl for spintronic and thermoelectric applications

Graphical abstract

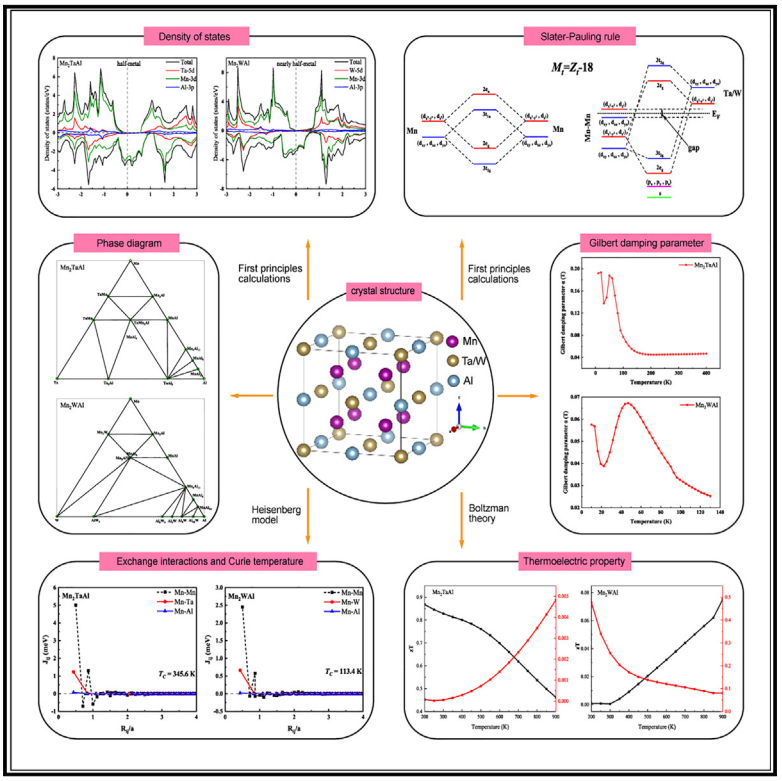

Highlights

- Mn_2TaAl and Mn_2WAl alloys are predicted to be half-metal and nearly half-metal
- Mn_2TaAl and Mn_2WAl alloys have a lower Gilbert damping parameter
- Total spin magnetic moments of Mn_2TaAl and Mn_2WAl alloys obey the $M_t = Z_t$-18 rule
- Thermodynamic properties of Mn_2TaAl and Mn_2WAl have an evident change at Curie point

Authors

Xiao-Ping Wei, Xin Liu, Jiao-Yang Zhang, Ya-Ling Zhang, Xiaoma Tao

Correspondence

weixp2008@lzjtu.edu.cn

In brief

Materials science; Materials property; Magnetic property; Thermal property

Wei et al., 2024, iScience 27, 111257
December 20, 2024
https://doi.org/10.1016/j.isci.2024.111257

CellPress

iScience

CellPress
OPEN ACCESS

Article

Investigations on full-Heusler alloys Mn_2TaAl and Mn_2WAl for spintronic and thermoelectric applications

Xiao-Ping Wei,[1,4,*] Xin Liu,[1] Jiao-Yang Zhang,[1] Ya-Ling Zhang,[2] and Xiaoma Tao[3]
[1]The School of Mathematics and Physics, Lanzhou Jiaotong University, Lanzhou 730070, P.R. China
[2]Institute of Modern Physics, Chinese Academy of Sciences, Lanzhou 730000, P.R. China
[3]College of Physical Science and Technology, Guangxi University, Nanning 530004, P.R. China
[4]Lead contact
*Correspondence: weixp2008@lzjtu.edu.cn
https://doi.org/10.1016/j.isci.2024.111257

SUMMARY

Half-metallic materials are widely used as spintronic devices such as electrodes, magnetic tunneling junction, and giant magnetoresistance. In this work, we have systematically investigated the structural stability, Gilbert damping, electronic structure, and magnetism together with exchange interactions and Curie temperatures for Mn_2TaAl and Mn_2WAl alloys. Initially, we estimate their structural stability and offer possible phase synthesis. Subsequently, the Gilbert damping parameters calculated by the linear response theory are used to assess their response speed as spintronic materials. Furthermore, the Mn_2TaAl and Mn_2WAl are predicted to be half-metallic and nearly half-metallic ferrimagnets and their total magnetic moments obey the $Mt = Zt$-18 rule. Accordingly, their Curie temperatures for Mn_2TaAl and Mn_2WAl are also evaluated by the mean-field approximation. Finally, their thermodynamic parameters within 0∼600 K and thermoelectric properties within 200∼900 K are discussed. Overall, our research for Mn_2TaAl and Mn_2WAl alloys might provide some valuable clues for their application in spintronic devices.

INTRODUCTION

Half-metal is defined as one of the spin configurations displaying the metallic behavior, and the other is the behavior of a semiconductor or insulator which leads to the conduction electrons fully polarized at the Fermi level. The unique character was first discovered when studying the band structure of NiMnSb.[1] Half-metallic (HM) spintronic devices such as magnetic tunnel junctions, electrodes, spin filters, and giant magnetoresistance exhibit many merits compared with conventional electronic devices, such as the stronger non-volatility, higher integration, faster data processing speed, and lower energy consumption.[2] Consequently, the HM materials represent a prospective avenue for the development of next-generation electronic devices.

In recent years, the half-metallicity is found among many materials, such as the metal oxides CrO_2, Fe_3O_4, $La_{0.7}Sr_{0.3}MnO_3$, Sr_2FeMoO_6 and $Sr_3Ru_2O_7$,[3–8] binary alloys,[9–12] and Heusler alloys.[13–20] Among the aforementioned materials, it is particularly interesting for Heusler alloys because of their structural compatibility with conventional semiconductor, as well as their potentially low Gilbert damping and high Curie temperature.[21–26]

Heusler alloys are divided into the full-Heusler and half-Heusler alloys,[27] their chemical formula are X_2YZ and XYZ, where X and Y are different transition metals (TMs), and Z is *sp* element. Full-Heusler alloys X_2YZ usually crystallize into the structures of $L2_1$ and Hg_2CuTi types; they have four positions of A (0, 0, 0), B (1/4, 1/4, 1/4), C (1/2, 1/2, 1/2) and D (3/4, 3/4, 3/4), respectively. The atomic occupations in Wyckoff positions are generally decided by the number of their outermost valence electrons; when the valence electron of X atom is greater than that of Y atom, the X atoms occupy the positions of A and C, forming the $L2_1$ structure.[28] Instead, the Hg_2CuTi structure is formed. Half-Heusler alloys with $C1_b$ structure is formed when one of X atoms in the full-Heusler X_2YZ is absent.

Until now, many Heusler alloys are predicted to be HM materials. Among these half-metallic materials, the Co_2-, Mn_2-, Fe_2- and Ni_2-based HM Heusler alloys attract widely attention.[24,29–33] Among them, the Mn_2-based Heusler alloys are concerned particularly due to their relatively low cost and plasticity. It is reported that the Mn_2VAl and Mn_2CrAl are half-metals with high Curie temperature,[34–36] and the Ta and V elements as well as Cr and W elements have the same outer valence electrons because of their same cycle, therefore, we want to know whether they are still half-metals when the V atom in Mn_2VAl or the Cr atom in Mn_2VAl is replaced by Ta or W atom. Another reason for the quest is to find the half-metal with high Curie temperatures, which is likely to be realized by changing the components of Heusler alloys and expanding the database of spintronic materials.

In the current work, we take the Mn_2TaAl and Mn_2WAl alloys as an object, and study their structural stability, Gilbert damping parameter, electronic structure and magnetic properties as

well as exchange interaction and Curie temperature since the Mn_2VAl alloy has been prepared in experiment.[37] The purpose is to provide theoretical guidance for the experimental synthesis of the two alloys and their application in spintronic devices. The manuscript is organized as follows: Section 2 provides calculation details, Section 3 displays the results and discussion, and Section 4 gives the summary and conclusions.

Calculation details

The full potential local orbital minimum basis code[38] was applied to calculate the electronic structure and magnetism of Mn_2TaAl and Mn_2WAl. The Perdew-Burke-Ernzerhof (PBE) parameterization in the framework of the generalized gradient approximation (GGA) is applied for scalar and fully relativistic calculations,[39] the Brillouin zone with a 30 × 30×30 *k*-points is used. The density functional theory with the spin in the VASP software package[40] and the projector-enhanced wave (PAW) potential[41] were used to calculate the stability, elastic constants, electron localization function and charge density, the PBE function is utilized to account for exchange correlation effects. The plane-wave cut-off energy was set to 600 eV and the Brillouin zone was sampled with Monkhorst-Pack grid.[42] The 20^3 *k*-points in the Brillouin zone are generated for lattice optimization.

In addition, the exchange interactions of Mn_2TaAl and Mn_2WAl alloys are obtained by Munich SPRKKR-program,[43] where the Fermi energy was determined by the Lloyd's formula.[44,45] The Vosko-Wilk-Nusair (VWN) correlation potential, l_{max} = 3 angular momentum cutoff and 22^3 mesh are employed when calculating the exchange coupling parameter[46] since the calculations of $Fe_{100}Z_x$ (Z = Ga, Ge, Al) indicate that the Curie temperature obtained by the LDA-VWN approximation is in good agreement with the that of experiment.[47]

The Hamiltonian (*H*) of system with spin is represented as follows:

$$H = -\sum_{i,j} e_i e_j J_{ij} \qquad \text{(Equation 1)}$$

where J_{ij} denotes the exchange interaction of the spins of sites *i* and *j*, e_i and e_j are the unit vectors of the magnetic moments at atomic sites *i* and *j*, J_{ij} is calculated by the LKAG formalism:[48–50]

$$J_{ij} = \frac{1}{\pi}\int_{-\infty}^{\varepsilon_F} \mathrm{Im}\mathrm{Tr}\left(\Delta_i \tau_{ij}^{\uparrow} \Delta_j \tau_{ji}^{\uparrow}\right) d\varepsilon \qquad \text{(Equation 2)}$$

where τ_{ij} and ε_F are the scattering path operator and the Fermi energy, respectively, and $\Delta_i = \boldsymbol{t}_{i,\uparrow}^{-1} - \boldsymbol{t}_{i,\downarrow}^{-1}$ means the spin-resolved difference of single-site scattering matrix t_i of site *i*. For the Mn_2TaAl and Mn_2WAl, we solve the following coupled equations:

$$\frac{3}{2}k_B T_C^{MFA}\langle e^{\mu}\rangle = \sum_{\nu} J_0^{\mu\nu}\langle e^{\nu}\rangle \qquad \text{(Equation 3)}$$

$$J_0^{\mu\nu} = \sum_{r\neq 0} J_{0r}^{\mu\nu} \qquad \text{(Equation 4)}$$

where e^{μ} is denoted as the average *z* component of the unit vector $\boldsymbol{e}_{\boldsymbol{r}}^{\boldsymbol{v}}$ from the direction of the magnetic moment of site ($\boldsymbol{v}$, $\boldsymbol{r}$). Equ. 3 is be rewritten as:

$$(\Theta - \mathrm{TI})\mathrm{E} = 0 \qquad \text{(Equation 5)}$$

$$\frac{3}{2}k_B\Theta_{\mu\nu} = J_0^{\mu\nu} \qquad \text{(Equation 6)}$$

The maximum eigenvalues of the Θ matrix are the Curie temperatures of two alloys. Calculation details can also be found in ref. 51–53 BoltzTraP is a modern implementation of the electronic energy band smoothing Fourier interpolation algorithm, which is the basis for the widely used original BoltzTraP code.[54] We make BoltzTraP compute the hotspot parameter, which enables Fourier expansion of the energy bands and special functions to preserve the symmetry of the space group.

RESULTS AND DISCUSSION

Crystal and stability

First, we model the structures of full-Heusler alloys Mn_2TaAl and Mn_2WAl as displayed in Figure 1, where the Mn atoms take up the Wyckoff positions of A and C, and the Ta or W atom is located in the B position, forming the $L2_1$ structure. Furthermore, we calculate the ferromagnetic total energies of both alloys, and fit their data of total energy and volume to determine their magnetic ground states, the fitted lattice parameters of ground state are listed in Table 1. On the basis of the magnetic ground states, we evaluate their structural stability and offer their possible phase synthesis.

The energy of formation E_f, which is used for the measurement of the thermodynamic stability, is defined as[55]

$$E_f = \frac{1}{N_{atom}}\left(E_{tot} - \sum_i \mu_i x_i\right) \qquad \text{(Equation 7)}$$

where E_{tot} is the total energy, μ_i and x_i denote the atomic chemical potential and the amount of the *i*th element, N_{atom} is the atomic number per formula unit, respectively. From the Table 1, we can see a negative E_f for Mn_2TaAl and Mn_2TaAl alloys, indicating that they are easier synthesized in experiment. To find most probably decomposition reaction, we also discuss the convex hull and phase separation for both alloys. Based on the database OQMD,[56] Mn_2TaAl is likely to decompose into binary $TaAl_3$, TaMn, Mn_2Al phases, and the Mn_2WAl is decomposed into Mn_2Al and W components, and their convex hulls are −1.393 and −1.364 eV/atom, respectively, as listed in Table 2. It is reported that Heusler alloys can be synthesized when their convex hulls are less than 0.1 eV/atom.[57] Therefore, Mn_2TaAl and Mn_2WAl alloys meet the thermodynamic stability, they are extremely possible synthesized in experiment because their convex hulls are very small. In addition, we also provide possible phase diagram for the synthesis of Mn_2TaAl and Mn_2WAl alloys in Figure 2 according to the database OQMD.[58]

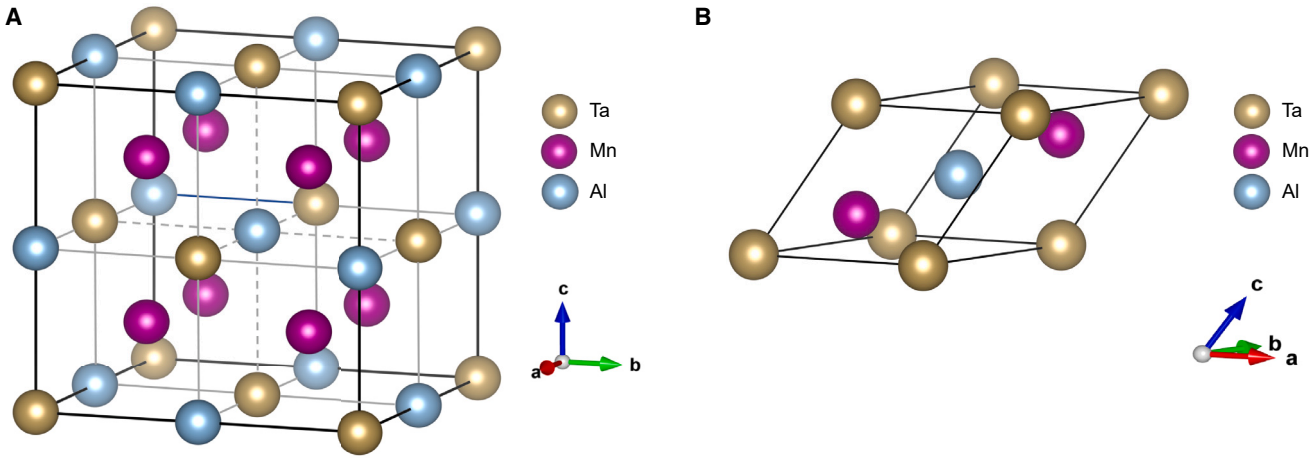

Figure 1. Unit cell and primitive cell of Mn2TaAl alloy
Crystal structure of Mn_2TaAl and Mn_2WAl alloys (A) unit cell and (B) primitive cell.

Subsequently, we assess the dynamical stability for Mn_2TaAl and Mn_2WAl. From the Figure 3, we see that the imaginary frequencies of phonon spectra for both alloys are absent, which means that they are dynamically stability. In addition, the fluctuations in total energy over time to estimate thermal stability. For the Mn_2TaAl and Mn_2WAl alloys, Figure 4 shows the curves of total energy versus time at 300 K and 100 K, implying that the two alloys satisfy the thermal stability by comparing the structures before and after the evolution.

Moreover, the elastic constants C_{ij} is calculated to measure the mechanical stability of both alloys by using the following formula:

$$C_{ij} = \frac{1}{V_0}\left(\frac{\partial^2 E}{\partial \varepsilon_i \varepsilon_j}\right) \quad \text{(Equation 8)}$$

where E and V_0 denote the internal energy and the volume at equilibrium, respectively, ε_i and ε_j denote the applied strains. The Born-Huang criteria in Equ. 9 can be used to evaluate the mechanical stability of Mn_2TaAl and Mn_2WAl:

$$B = \frac{C_{11}+2C_{12}}{3} > 0 \quad \text{(Equation 9)}$$

$$C_{11} - C_{12} > 0$$

$$C_{44} > 0$$

based on the elastic constants in Table 1, we conclude that Mn_2TaAl and Mn_2WAl satisfy the mechanical stability. Besides, we also derive the elastic properties from the elastic constants, such as the bulk modulus B and the shear modulus G using the Equations 10, 11, and 12:[59]

$$B = \frac{C_{11}+2C_{12}}{3} \quad \text{(Equation 10)}$$

$$G_R = \frac{5C_{44}(C_{11} - C_{12})}{4C_{44}+(C_{11} - C_{12})} \quad \text{(Equation 11)}$$

$$G_V = \frac{C_{11} - C_{12}+3C_{44}}{5} \quad \text{(Equation 12)}$$

where G_R and G_V denote the Reuss and the Voigt shear moduli, respectively, the value of Voigt-Reuss-Hill is approximation obtained by their arithmetic mean:[60]

$$G = \frac{G_V + G_R}{2} \quad \text{(Equation 13)}$$

the Young's modulus E, Poisson's ratio v, anisotropy factor A, and average sound velocity v_m are obtained:[61]

$$E = \frac{9BG}{3B+G} \quad \text{(Equation 14)}$$

$$v = \frac{3B - 2G}{2(3B+G)} \quad \text{(Equation 15)}$$

Table 1. Calculated lattice parameters a_{cal} (Å), formation energy E_f (eV/atom), elastic constants C_{ij} (GPa), bulk modulus B (GPa), shear modulus G (GPa), Pugh's criteria B/G, Young's modulus E (GPa), Poisson's ratio v, anisotropy factor A, average sound velocity v_m, melting temperature T_{melt} (K) of Mn_2TaAl and Mn_2WAl alloys are shown

Alloys	a_{cal}	E_f	C_{11}	C_{12}	C_{44}	B	G	B/G	E	v	A	v_m	T_{melt}
Mn_2TaAl	6.011	−0.423	359.170	132.830	98.200	208.270	141.840	1.470	346.800	0.223	0.868	132.488	2543.983
Mn_2WAl	5.989	−0.394	411.630	157.350	114.180	242.110	161.770	1.500	396.910	0.227	0.898	137.628	2858.616

Table 2. Most likely decomposition reaction, and the decomposition energy ΔH along with convex hull in Mn_2TaAl and Mn_2WAl alloys

Decomposition reaction	ΔH (eV/atom)[a]	Convex hull (eV/atom)
$7Mn_2TaAl \rightarrow 4Mn_2Al + TaAl_3 + 6TaMn$	−0.299	−1.393
$Mn_2WAl \rightarrow Mn_2Al + W$	−0.213	−1.364

[a]ref. 47.

$$A = \frac{2C_{44}}{C_{11} - C_{12}} \quad \text{(Equation 16)}$$

$$v_m = \left[\frac{1}{3}\left(\frac{2}{v_s^3} + \frac{1}{v_l^3}\right)\right]^{-\frac{1}{3}} \quad \text{(Equation 17)}$$

$$v_l = \left(\frac{3B + 4G}{3\rho}\right)^{\frac{1}{2}} \quad \text{(Equation 18)}$$

$$v_s = \left(\frac{G}{\rho}\right)^{\frac{1}{2}} \quad \text{(Equation 19)}$$

We have tabulated the calculated E, v, A and v_m in Table 1. The compressive strength of a material is quantified by B, the stiffness is provided by E. It can be observed that the higher the value of E, the stiffer the material. Poisson's ratio, represented by the symbol v, is applied to measure the ratio of lateral contraction to longitudinal elongation in elastic direction. The majority of metals exhibit v values of approximately 0.25, the v values of two alloys are smaller than those of metals. In particular, the A values for Mn_2TaAl and Mn_2WAl deviate from one, indicating the anisotropy of C_{ij}. Accordingly, we also offer the two- and three-dimensional B, E, G and v of Mn_2TaAl and Mn_2WAl in Figure 5, it is obvious that these parameters show significant anisotropic behavior except for the bulk modulus. Based on the Pugh's criteria,[62] the material exhibits the ductility when B/G > 1.75, vice versa, indicating the brittleness, we find that both alloys have a brittle behavior according to the B/G value. Furthermore, the melting temperature T_{melt} of Mn_2TaAl and Mn_2WAl is obtained by the following equation:[63]

$$T_{melt} = 607 + 9.3 \times B \pm 555 \quad \text{(Equation 20)}$$

We can see that the T_{melt} of Mn_2WAl is higher than that of Mn_2TaAl because of its larger B.

The bonding properties can be characterized by the v. For the ionic behavior, this ratio is equal to 0.25, while for metallic or covalent behavior, it is greater than or less than 0.25,[64] respectively. For Mn_2TaAl and Mn_2WAl alloys, the ratio is less than 0.25, indicating their covalent behavior (see Table 1). The Kleinmen parameter ζ is used to describe the stretching and bending of bond. A value of ζ equal to zero indicates the minimization of bond bending, whereas a value of ζ equal to one represents the minimization of bond stretching.[65] It can be seen from Table 3 that the ζ about 0.5 implies a bond bending of the alloys. Additionally, the Vickers hardness H_v is employed to characterize the ductility and brittleness of material, the H_v of a material represents its intrinsic resistance to deformation.[66] In general, the higher the hardness of the material is, the higher the brittleness is. The calculated hardness proves the reliability of the results of ductility or brittleness, indicating that the Mn_2WAl alloy is more brittle than that of Mn_2WAl. In addition, the compressibility and the shear stiffness of material are measured through the first and second Lames constants (λ, μ).[67]

$$\zeta = \frac{C_{11} + 8C_{12}}{7C_{11} + 2C_{12}} \quad \text{(Equation 21)}$$

$$\lambda = \frac{E_v}{(1+v)(1-2v)} \quad \text{(Equation 22)}$$

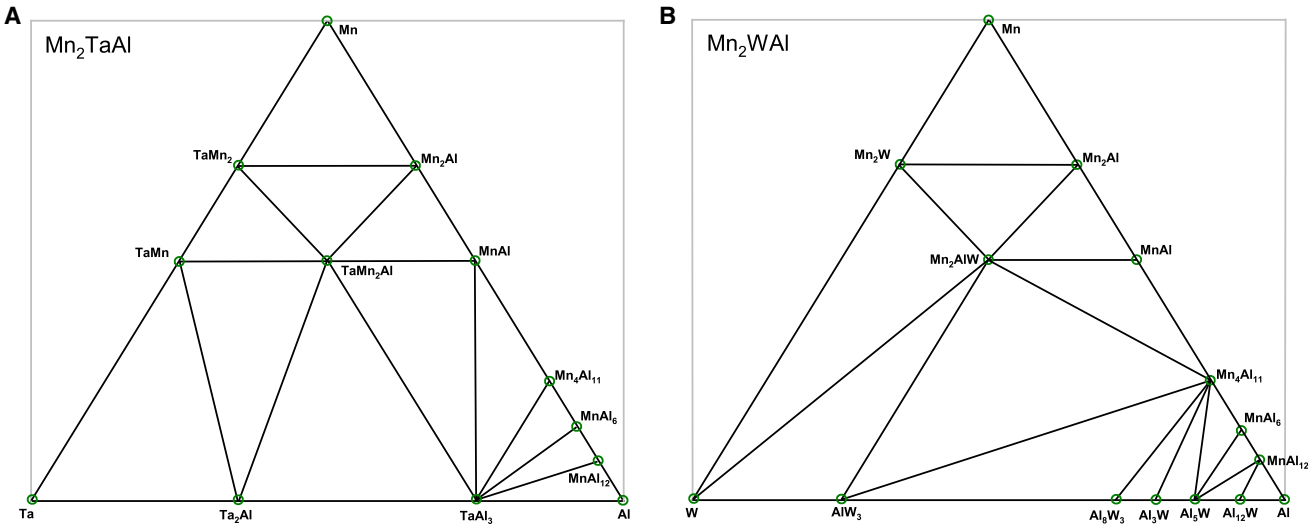

Figure 2. The phase diagram of a ternary Ta/W-Mn-Al system

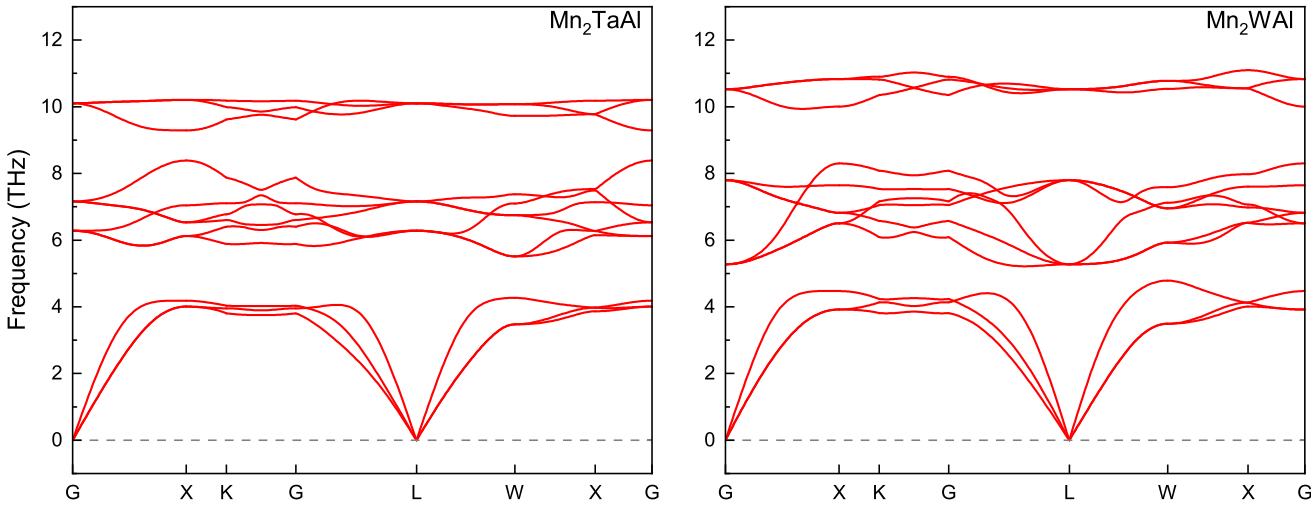

Figure 3. Calculated phonon spectrums for Mn_2TaAl and Mn_2WAl alloys

$$\mu = \frac{E}{2(1+v)} \quad \text{(Equation 23)}$$

$$H_v = \left[\left(\frac{G}{B}\right)^2 \times G\right]^{0.585} - 3 \quad \text{(Equation 24)}$$

Gilbert damping parameters

In order to improve the data access time of magnetic memories, replacing level caches and temporary memories of current CMOS-based computing, faster magnetization reversal must be realized, which requires ferromagnets with lower Gilbert damping constants,[68] and the value of Gilbert damping constant becomes an important indicator for the reduction of the switching current.

Subsequently, the Gilbert damping constant, which is derived from the electronic structure of the Green's function $G+(E)$, is calculated through using linear response theory, and can be obtained in an efficient method through the utilization of the spin-polarized relativistic of multiple scattering theory.[69] The diagonal elements $\mu = x, y, z$ of the Gilbert damping tensor can be expressed as:

$$\alpha^{\mu\mu} = \frac{g}{\pi m_{tot}} \sum_j Tr\left\langle T_0^{\mu} \tilde{\tau}_{0j} T_j^{\mu} \tilde{\tau}_{j0} \right\rangle_c \quad \text{(Equation 25)}$$

where the factor g is $2(1+m_{orb}/m_{spin})$, m_{tot} is the sum of the m_{spin} and m_{orb}, where m_{spin} and m_{orb} are spin and orbital magnetic

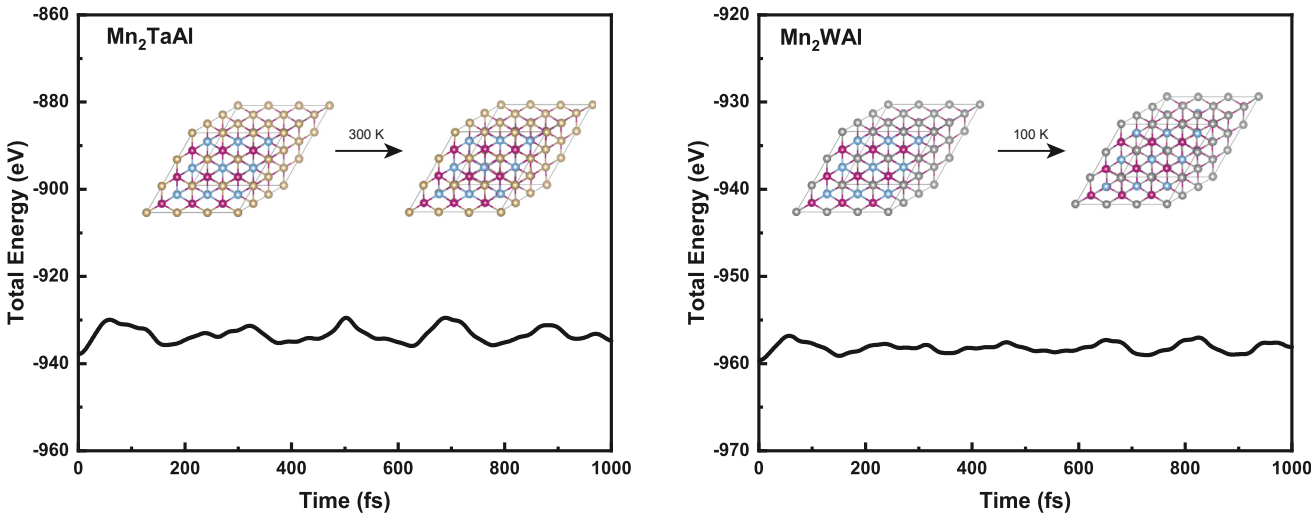

Figure 4. Evolution curve of total energy with time for Mn_2TaAl and Mn_2WAl alloys at 300 K and 100 K

Note that the inserted pictures are before and after evolutionary structures

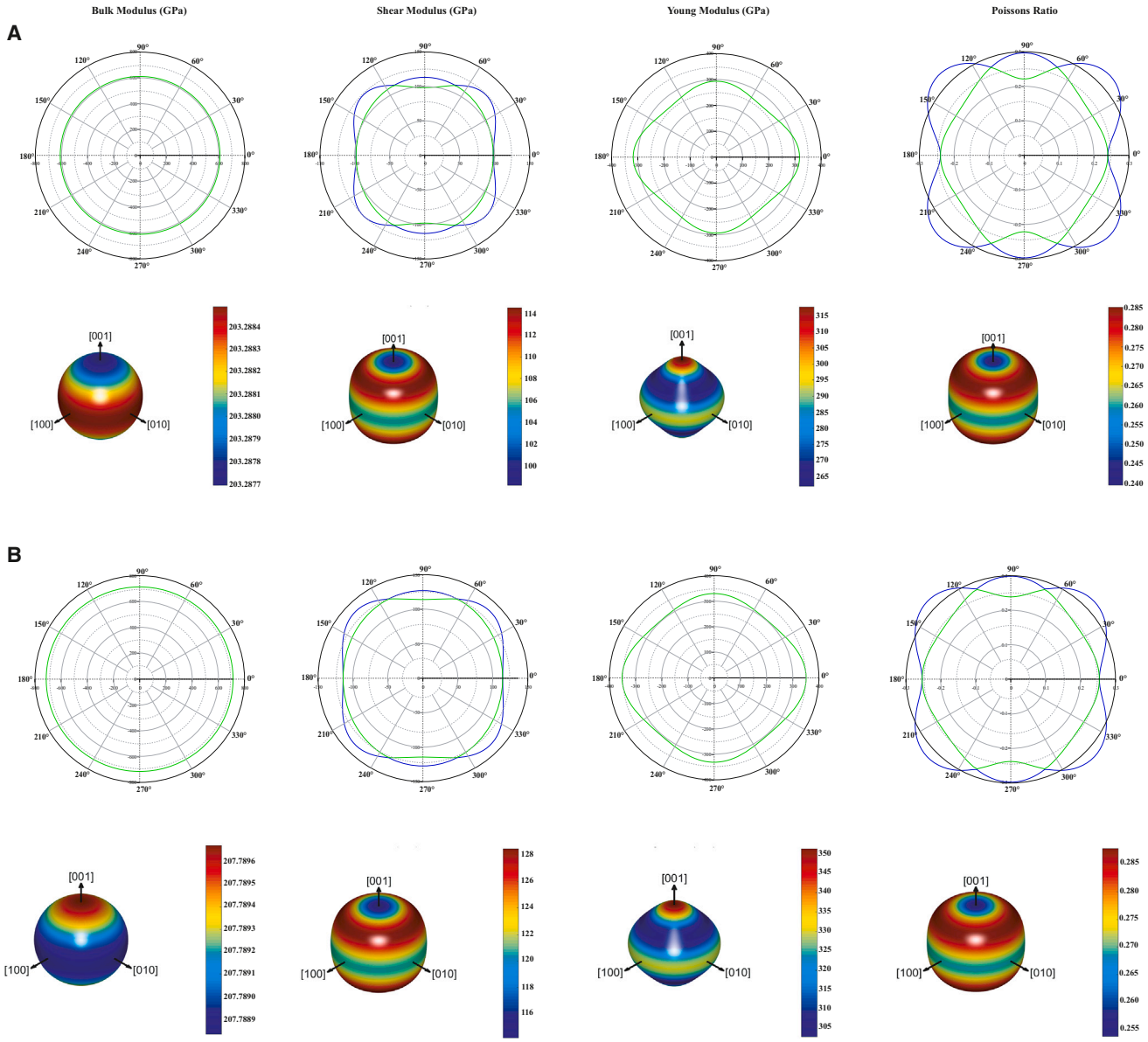

Figure 5. Elastic properties of Mn2TaAl and Mn2WAl alloys

2D and 3D bulk modulus, shear modulus, Young's modulus and Poisson's ratio of (A) Mn_2TaAl and (B) Mn_2WAl alloys.

moments per formula unit. Equation 25 gives an $\alpha^{\mu\mu}$ at site 0, and total contribution from all positions that have been indexed by j, containing those with the value of $j = 0$. $\tilde{\tau}_{ij}$ is provided by the imaginary part of the multiple scattering operator. $\boldsymbol{T}_i^{\mu}$ is represented as $\widehat{T}^{\mu} = \beta(\vec{\sigma}\times\hat{m}_z)_{\mu}B_{xc}(\vec{r})$.[70] The symbol$\langle\cdots\rangle$denotes the configurational averages with the vertex corrections.[71] Usually, the $\alpha^{\mu\mu}$ with the vertex correction is more accurate than the one without the vertex correction as it takes into account the "scattering" in the Boltzmann equation, and corrects for damping errors. In Figure 6, we give the $\alpha^{\mu\mu}$ with vertex corrections. Normally, the $\alpha^{\mu\mu}$ is determined by a combination of the spin-orbit coupling (SOC) strength and the density of states (DOS) at the Fermi energy level (E_F). However, the SOC in cubic crystals can be omitted due to orbital quenching (see Table 4). Therefore, $\alpha^{\mu\mu}$ is only proportional to the value of DOS at the E_F. As illustrated in Figure 6, the Gilbert damping exhibit a comparable pattern temperature, namely, there is an evident decrease for $\alpha^{\mu\mu}$ within 0∼20 K, implying a sudden decrease for DOS at the E_F, and then increases in 20–50 K, and finally decreases and plateau with increasing the temperature above 50 K, the peak at 50 K shows a strong scattering. The $\alpha^{\mu\mu}$ values in Mn_2TaAl and Mn_2WAl alloys are 0.047 and 0.026 at 300 K and 100 K, respectively. Therefore, we expect that Mn_2TaAl and Mn_2WAl have a less response time in magnetic memories.

Table 3. Magnetic moments (μ_B), Kleinmen parameter ζ, Lames constants (λ, μ), Vickers hardness H_v, Gilbert damping parameters α (300 K), and Curie temperatures T_C (K) of Mn_2TaAl and Mn_2WAl alloys are shown

Alloys	M_t	Ta/W	Mn	Al	ζ	λ	μ	H_v	α	T_C^{MFA}
Mn_2TaAl	1.999	−0.489	1.298	−0.107	0.511	113.730	31.560	8.577	0.047	345.6
Mn_2WAl	0.999	−0.381	0.719	−0.058	0.523	134.290	36.690	9.228	0.026	113.4

Electronic structure and magnetic moment

In this section, we talk over the electronic and magnetism of Mn_2TaAl and Mn_2WAl. Firstly, we show the total and resolved DOS in Figure 7, it is clear the Mn_2TaAl exhibits the HM property because there is a metallic nature in minority-spin configuration, and semiconducting nature in majority-spin direction. However, for the Mn_2WAl, it is a nearly half-metal, it is because the bands pass through the E_F of spin configurations, and the DOS of majority-spin states at the E_F close to zero. Subsequently, we illustrate in detail the electronic distribution for both alloys. In terms of the DOS of Mn_2TaAl, the pseudo energy gap exists at 1 eV and −0.4 eV of minority-spin states, the Mn-3*d* states give a main contribution to total DOS within −3.0∼2.0 eV in spin directions, it is the Ta-5*d* states between 2 eV–3 eV, the Al-3*p* states provide a small contribution. In particular, the Mn-3*d* states show the strong localization because of their sharp and large peaks around the E_F, and display the hybridization with Ta-5*d* states due to their peaks in the same energy. While for the Mn_2WAl, the contribution from the Mn-3*d* states is relatively large, especially around the E_F, and the W-5*d* states play a leading role below −2 eV. In addition, we also find that the shape and hybridization of the total and orbital DOS are similar to those of Mn_2TaAl, suggesting that the band gap is led to the hybridization between *d*-*d* orbitals. The contribution from the Al-3*p* states is very small, but it offers the *p*-*d* occupation stabilizing the system.

The Mn_2TaAl and Mn_2WAl alloys include the strongly correlated 3*d*ays electrons, so it is necessary to account for the Coulomb repulsion of these electrons. In addition, DFT calculations usually underestimate the gap of the alloys. Hence, we recalculate the electronic states of Mn_2TaAl and Mn_2WAl in the framework of PBE+U, PBE+SOC and PBE+U+SOC for comparison. For the PBE+U calculation, we add the U term at U = 0.46 eV for the W-5*d* electron and U = 0.78 eV for the Mn-3*d* electron, and U = 0.43 eV for the Ta-5*d* electron, where we need to emphasize that the choice of U values is based on the Slater-Condon parameters.[72] The gap of Mn_2TaAl alloy is 0.68 eV in the scheme of PBE+U, which is larger than 0.3852 eV in the framework of PBE, implying that Mn_2TaAl retains its HM nature. For the Mn_2WAl alloy, its spin polarizations are 91.83% and 97.76% in the scheme of PBE and PBE+U, thus the HM behavior is not observed. In addition, we note that the localization of TDOS for both alloys is effectively reduced due to the SOC effect.

Under the PBE+SOC approach, the spin of the electron is no longer a good quantum number, thus preventing the electron eigenfunctions from maintaining the spin degrees of freedom. This leads to the majority-spin wavefunction in the HM gap having a partially minority-spin character, thereby destroying HM behavior. In general, the Heusler alloys with heavier element will cause a much higher spin-orbit induced DOS within the gap.[73] Another consequence of the SOC induces the emergence of orbital moment, which are very small due to orbital quenching. Based on the aforementioned analysis, we show the impact of SOC on the DOS of Mn_2TaAl and Mn_2WAl alloys. As illustrated in Figure 8, the DOS with SOC considered is almost identical to the DOS without SOC. In this case, the half-metallicity of

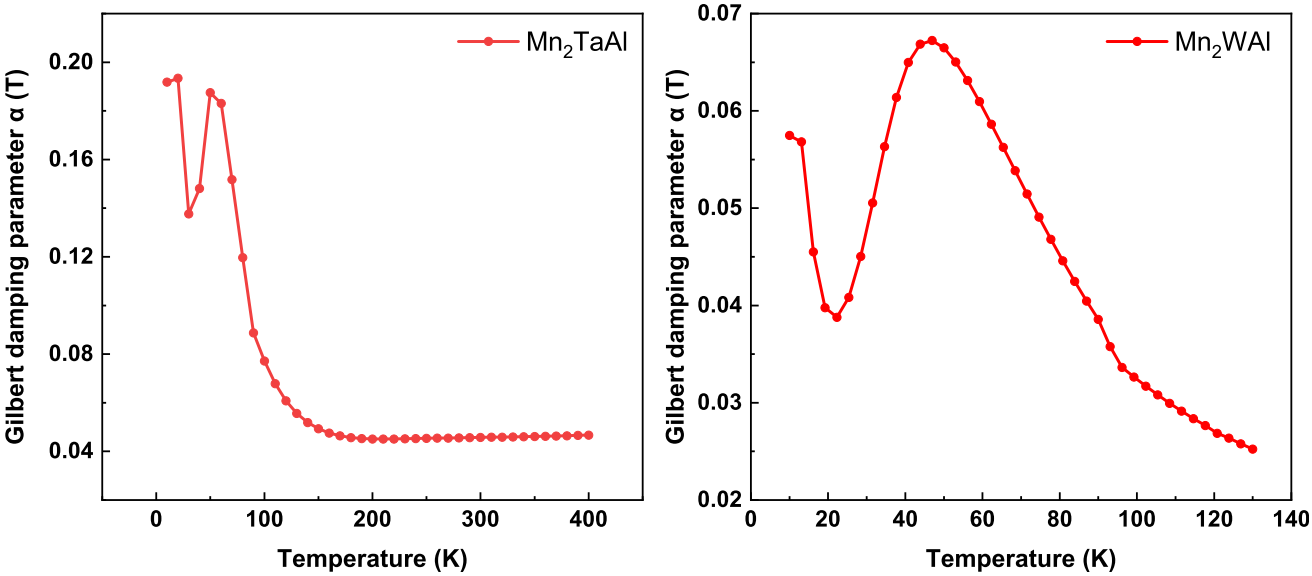

Figure 6. Gilbert damping parameters of Mn_2TaAl and Mn_2WAl alloys as a function of temperature are exhibited

Table 4. Comparison of magnetic moments (μ_B) of Mn_2TaAl and Mn_2WAl alloys calculated by PBE, PBE+U and PBE+SOC methods

Methods	Mn	Ta	Al	Total	Mn	W	Al	Total
PBE	1.30	−0.49	−0.11	2.00	0.72	−0.38	−0.06	1.00
PBE+U	1.30	−0.49	−0.11	2.00	0.73	−0.39	−0.06	1.01
PBE+SOC	1.30 (0.03)	−0.49 (0.03)	−0.11 (−0.001)	2.00 (0.09)	0.71 (0.02)	−0.37 (0.02)	−0.06 (0.001)	1.00 (0.07)

Note: the orbital magnetic moments of each atom are indicated in parentheses

Mn_2TaAl and Mn_2WAl is wrecked, and their spin polarizations are 97.50% and 89.90%, respectively. Furthermore, the magnetic moments with SOC considered are essentially unchanged, and the orbital moments of both alloys close to zero, as listed in Table 4. Finally, we discuss the effect of PBE+U+SOC on the electronic structure of Mn2TaAl and Mn2WAl alloys as shown in Figure 8, and found that their spin polarizations are 97.82% and 95.26%, respectively. The atomic magnetic moments under the PBE+U+SOC effect are almost unchanged in comparison with those of the PBE+SOC effect, while the orbital magnetic moments of transition metal atoms are slightly increased as listed in Table 4.

To study the bonding characterization of Mn_2TaAl and Mn_2WAl, the electron localization function (ELF) is displayed in Figure 9; it is a helpful tool for the description of the distribution of electrons in solids or molecules. A high ELF values indicate the presence of covalent bonds, nuclear or lone pairs of electrons, and the defective electrons or ions or metal bonds are typical of low values. The value of ELF ranges from 0 to 1, with an upper limit of 1, implying that the electrons are fully localized. ELF = 1/2 means that the electrons form an electron pair alike to that of an electron gas at that location.[74] Here, the ELF maps and line profiles of atoms are reduced by 2.5 times as presented in Figure 9. For the Mn_2TaAl, the mean value of ELF between Mn and Al atoms is 0.35, implying the occurrence of strong covalent bonding. The value of ELF between Mn and Mn atoms as well as Ti and Al atoms is only 0.15, suggesting the presence of metal or ionic bonds. The value of ELF between Ta and Mn atoms is 0.1, indicating the presence of metal or ionic bonds. For the Mn_2WAl, the ELF value between Mn and Al atoms is 0.3, meaning the appearance of strong covalent bonding, and the value between Mn atoms as well as W and Al atoms is 0.2, suggesting

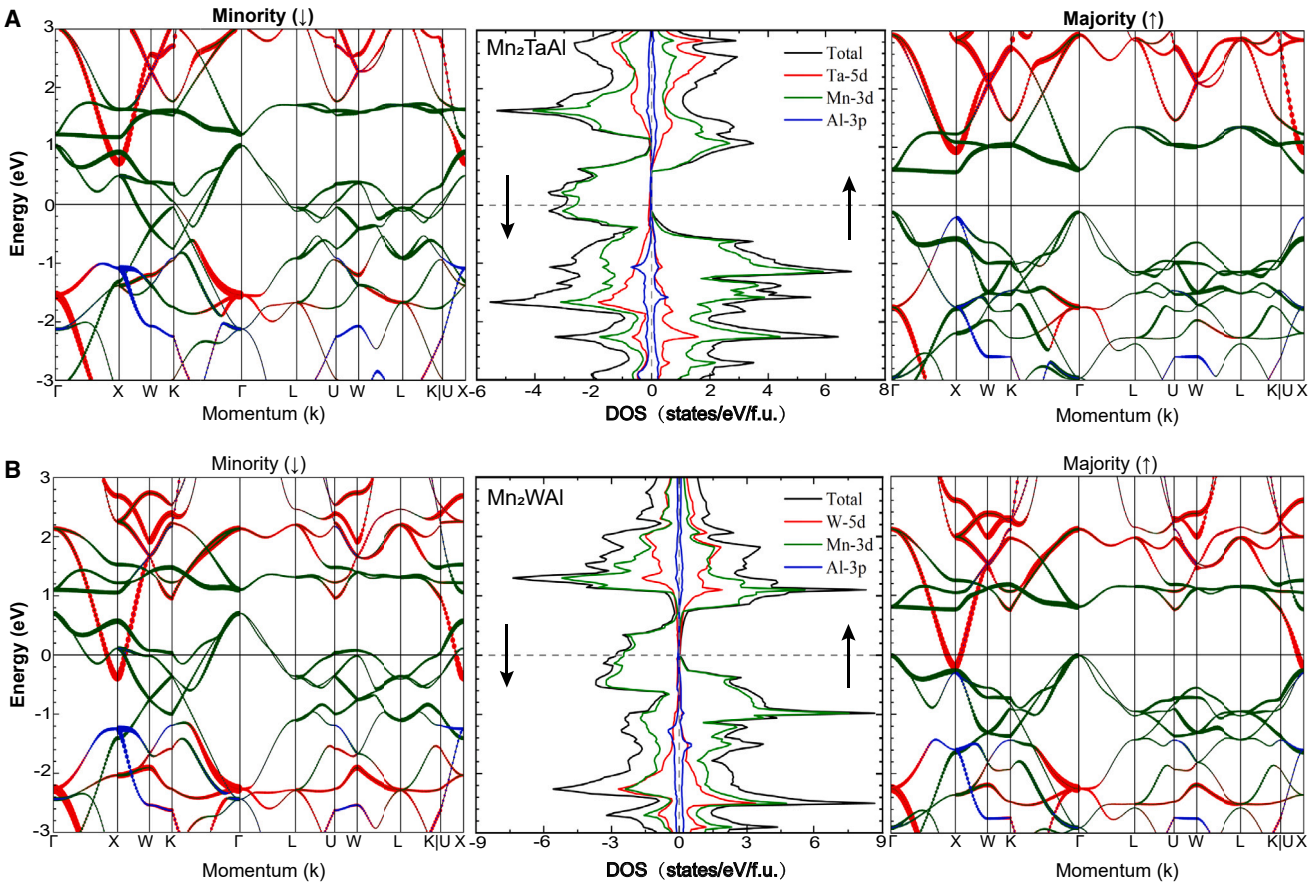

Figure 7. Total and orbital densities of states and energy bands of Mn_2TaAl and Mn_2WAl alloys

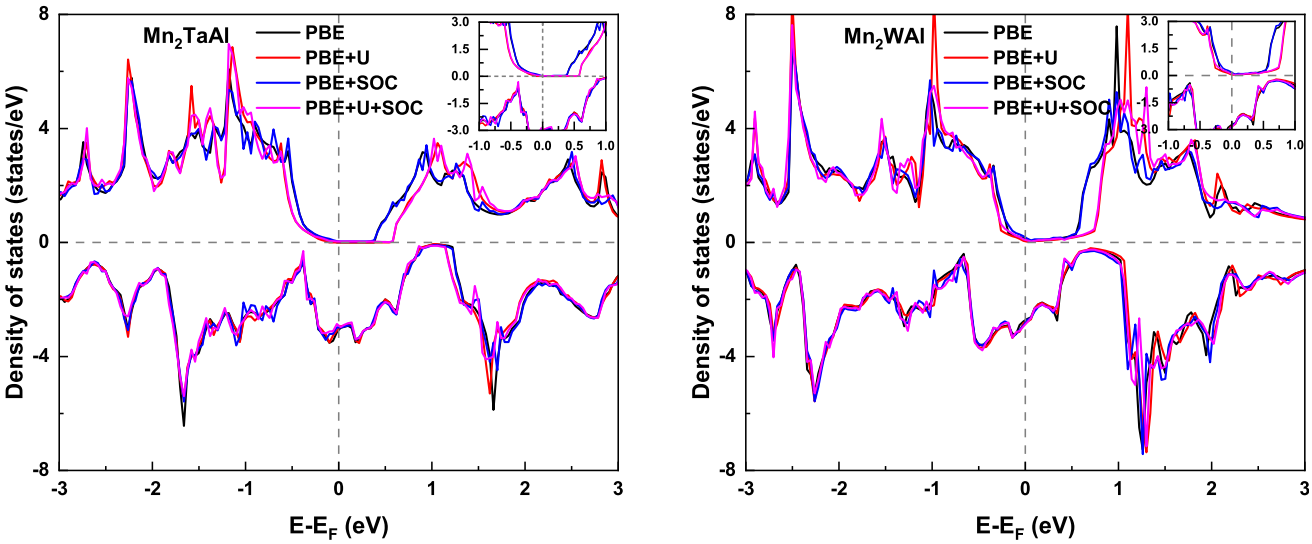

Figure 8. Total density of states of Mn_2TaAl and Mn_2WAl alloys in the schemes of adopts PBE, PBE+U and PBE+SOC methods

a covalent bond. However, the ELF between W and Mn atoms is only 0.13, indicating a metallic or ionic bond.

In the following, we discuss the bonding and anti-bonding through the Crystal Orbital Hamilton Population (COHP),[75] which decomposes the band into the pairwise interaction of the orbits and are chemically bond-weighted DOS between neighboring atomic pairs. The COHP is used to describe as the negative value of DOS multiplied by the corresponding Hamiltonian

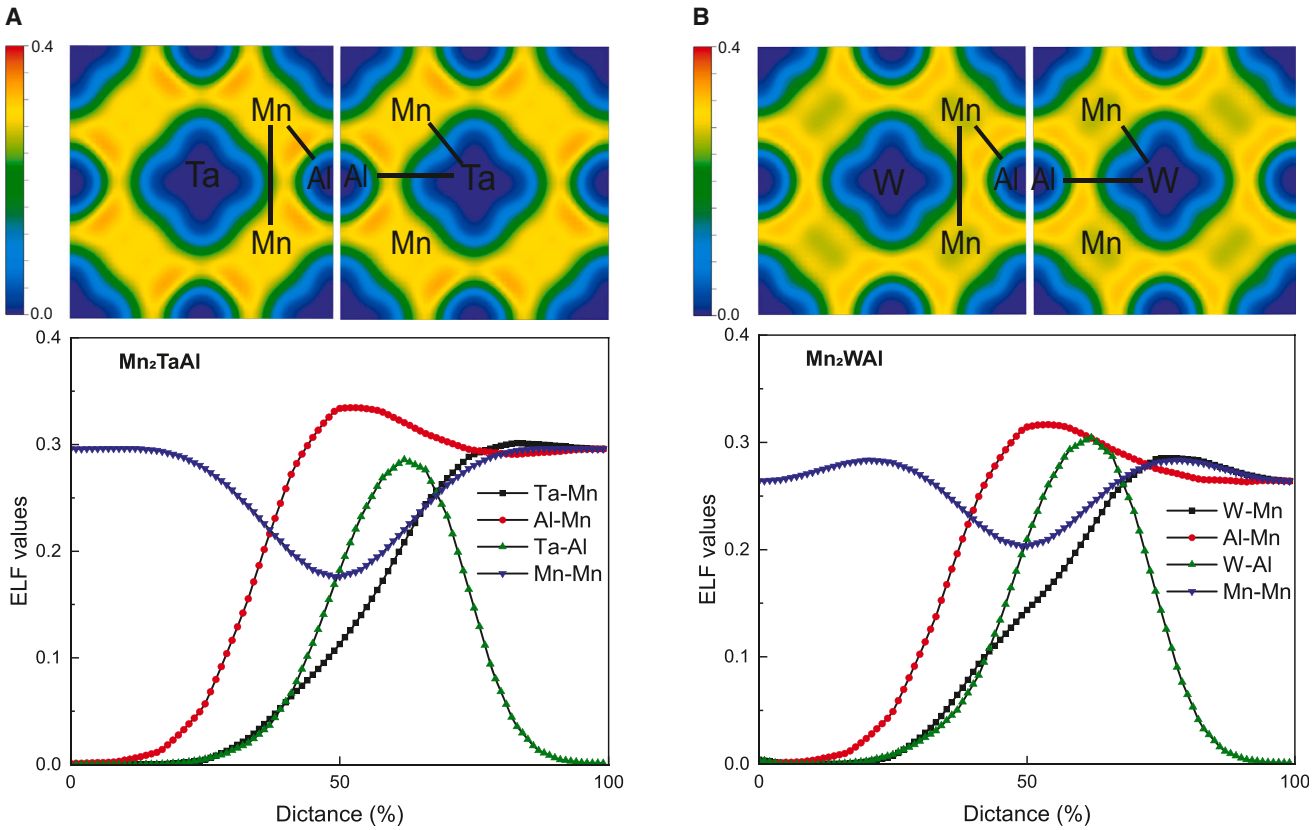

Figure 9. Electron localization function and the profile lines of Mn_2TaAl and Mn_2WAl alloys

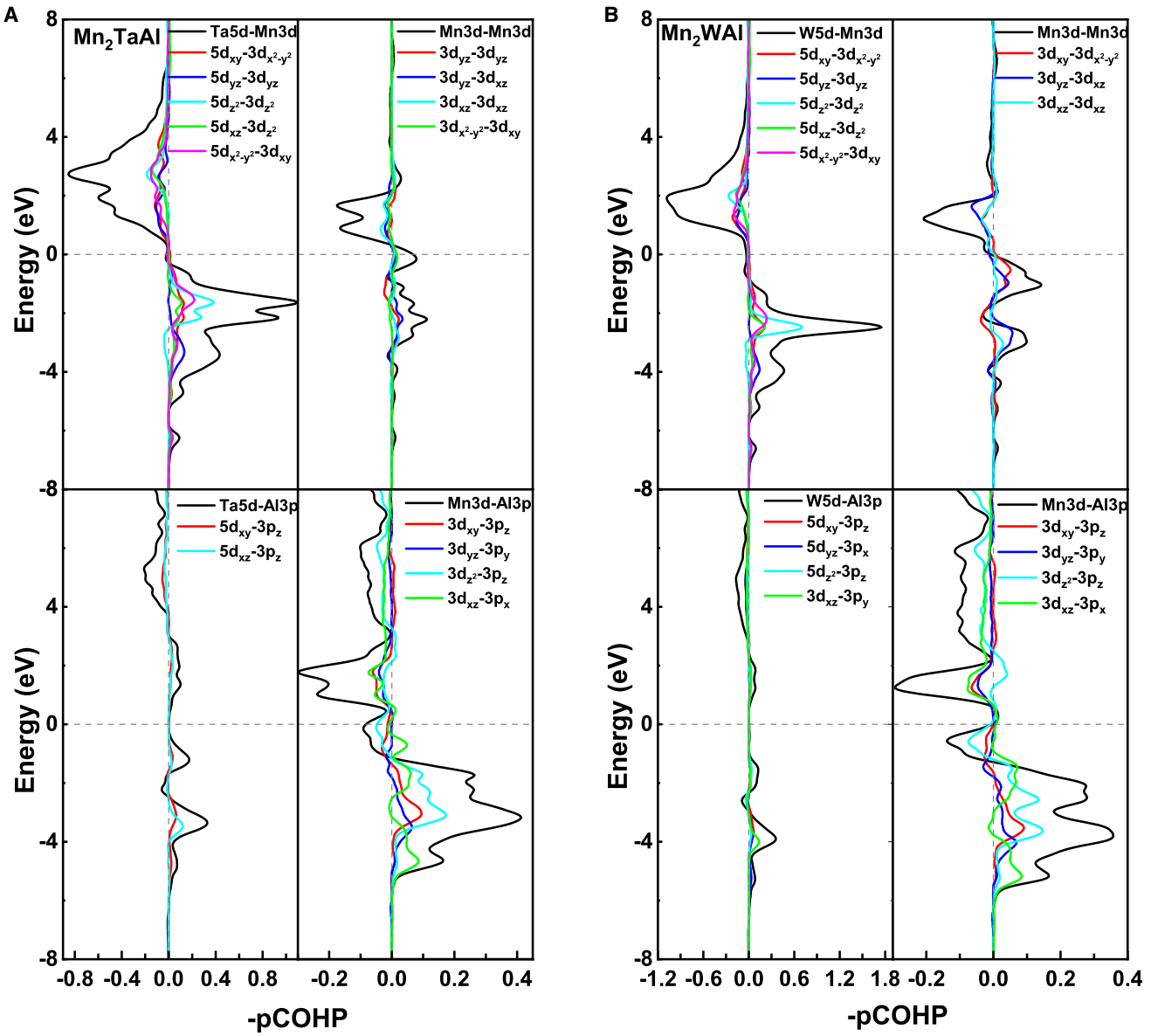

Figure 10. Crystal Oribital Hamilton Population of Mn2TaAl and Mn2WAl alloys

Calculated Crystal Orbital Hamilton Population of (A) Mn_2TaAl and (B) Mn_2WAlat the equilibrium state.

matrix element and shows the contribution from the bonding and anti-bonding states to the bands. A negative value of COHP indicate bonding states, and the anti-bonding states to the bands. A negative value of COHP indicate bonding states, and the anti-bonding states is a positive value. In Figure 10, we show the image of COHP, it can be seen that the 5*d* and 3*d* orbitals play a major contribution whether bonding or anti-bonding states, and induce the origin of HM gap. The integral values of COHP between atoms are presented in Table 5, we can see that in the Mn_2TaAl alloy, the bonding of Ta-Mn atoms is stronger than that of others, followed by the Mn-Al atoms, and the Mn - Mn bond is the weakest bonding. In the Mn_2TaAl alloy, the bonding states of Mn-W atoms are the strongest, followed by Mn-Al atoms, and it is the weakest for Mn - Mn atoms.

Table 5. Crystal Orbital Hamiltonian groups for Mn_2TaAl and Mn_2WAl alloys

Materals	Mn_2TaAl				Mn_2WAl			
Bonds	Ta-Mn	Mn-Mn	Ta-Al	Mn-Al	W-Mn	Mn-Mn	W-Al	Mn-Al
ICOHP	−1.327	−0.247	−0.653	−1.244	−1.400	−0.273	−0.628	−1.290

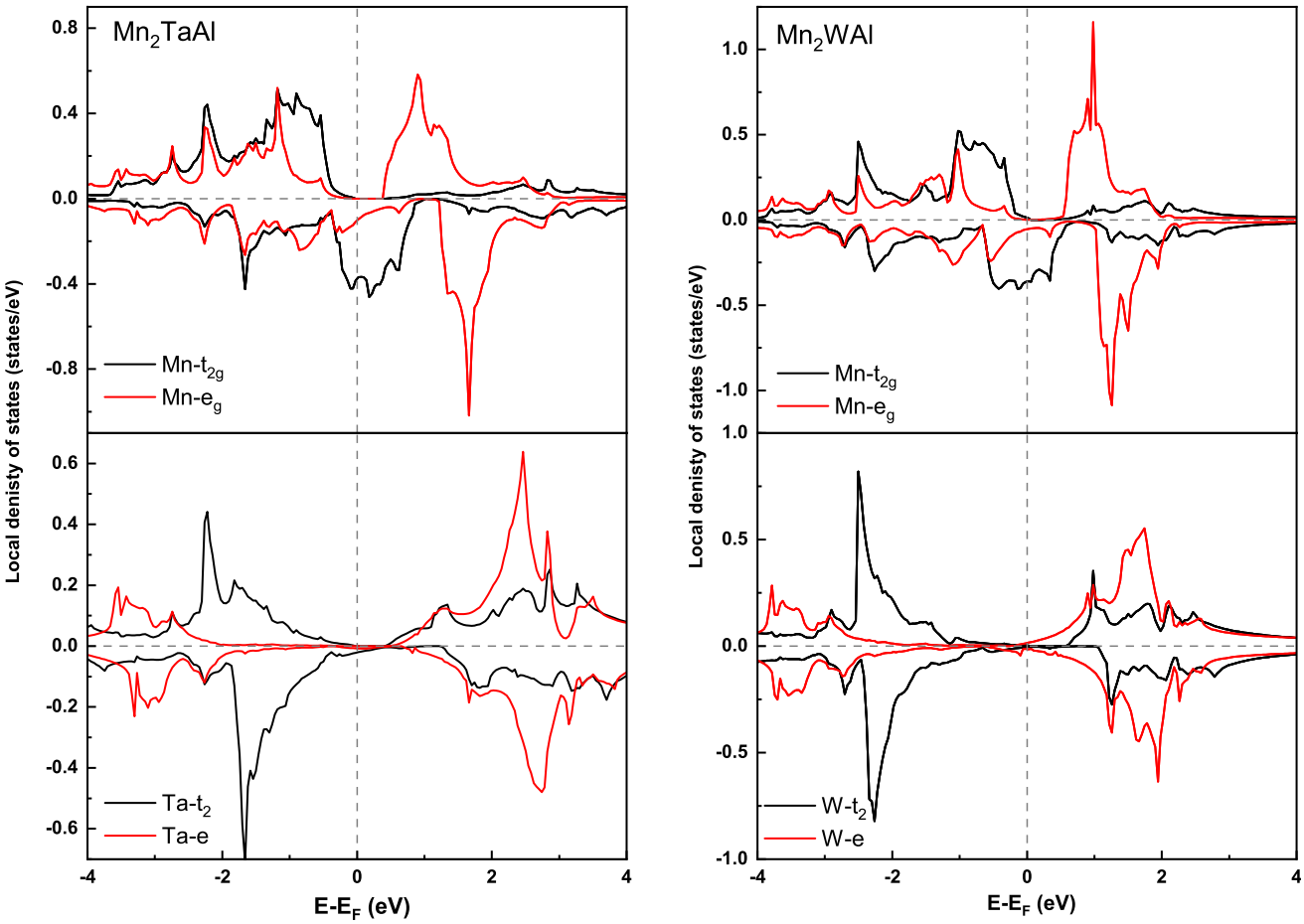

Figure 11. Localized density of states for transition metal *d* orbitals in Mn_2TaAl and Mn_2WAl alloys

Subsequently, the origin of HM gap is discussed through local density of states (LDOS) as displayed in Figure 11. Here, let us take the Mn_2TaAl to discuss it, the Mn-*d* states in the octahedral field are split into d_{xy}, d_{xz}, and d_{yz} states, and they are triple-degenerate and called the t_{2g} states, and the double-degenerate d_{z^2} and $d_{x^2-y^2}$ states, known as the $e_{.g.,}$ states, and the t_{2g} states are lower in energy than those of $e_{.g.,}$. The Ta-*d* states in the tetrahedral field are split into the d_{xy}, d_{xz}, and d_{yz} states, they are also triple-degenerate, and called the t_2 states, and the d_{z^2} and $d_{x^2-y^2}$ states with double-degenerate called the *e* states, and the t_2 states in energy are higher than the *e* states. From the Figure 11, we can see that the exchange splitting from t_{2g} and $e_{.g.,}$ states as well as t_2 and *e* states are responsible for the HM gap. Similarly, the conclusion can also be made for Mn_2WAl.

Whether the difference spin charge density plays also a role in the formation of HM gap, the difference spin charge density for Mn_2TaAl and Mn_2WAl alloys is displayed in Figure 12, it is

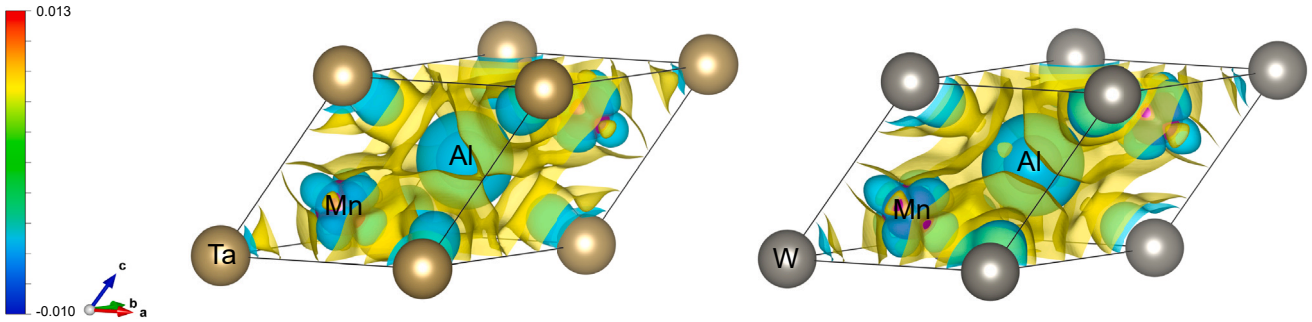

Figure 12. Spin differential charge density for Mn_2TaAl and Mn_2WAl alloys

Table 6. Bader charge analysis of Mn_2TaAl and Mn_2WAl alloys (+ means losing electrons, − means gaining electrons)

Alloys	Ta/W	Mn	Al
Mn_2TaAl	+0.391	−0.785	+1.177
Mn_2WAl	−0.258	−0.654	+1.567

found that the Mn atom accumulates the electrons from the Ta/W and Al atoms, which is good consistent with the calculated Bader charge (see Table 6), i.e., Mn atoms accumulate the electrons, and the Al atoms lose the ones. In particular, the Ta atom loses the electrons, and the W atom gains the electrons. We can therefore suppose that the charge transfer plays a partial role in forming the HM gap. Finally, we can conclude that the *d-d* bonding and anti-bonding states, the spin charge transfer and exchange splitting of *d-d* orbitals work together to form the HM gap.

Finally, we concern the magnetic moments for Mn_2TaAl and Mn_2WAl, it is found that the total magnetic moments comply with the Slater-Pauling rule:[76,77] $M_t = Z_t - 18$ because their outer valence electrons can be treated as itinerant electrons, where M_t stands for the total magnetic moments (in μ_B units), Z_t represents the total number of valence electron. There is an integral value of 2 μ_B and 1 μ_B in Mn_2TaAl and Mn_2WAl alloys (see Table 3). M_t can be interpreted by the *d*- and *p*-orbitals electrons occupation in the crystal field as displayed in Figure 13. First, the octahedrally symmetric Mn atoms hybridize with each other to form the t_{2g} and $e_{.g.,}$ bonding states and the t_{1u} and e_u non-bonding states. Furthermore, these bonding *d*-states hybridize with the Ta/W-*d* orbitals to produce bonding and anti-bonding states again. The Al atom also gives a single *s* state and triple-degenerate p_x, p_y and p_z states, which partially accommodate the charge of the *d* orbitals. Finally, there are nine occupied states, so that their total magnetic moment satisfies the $M_t = Z_t - 18$ rule. In fact, the rule is also reported in two literatures. Apart from this, we can also see in Table 4 that the M_t is mainly contributed by the Mn atoms, with 1.3 and 0.72 μ_B in Mn_2TaAl and Mn_2WAl alloys, respectively, followed by the Ta and W atoms, the magnetic moments are −0.49 and −0.38 μ_B, and the Al atoms show a very small magnetic moments because they are completely unpolarized, also, this is confirmed by the spin charge density shown in Figure 14. Namely, atomic magnetic moments are primarily carried by Mn atoms.

Exchange interaction and Curie temperature

To discuss the exchange interactions and the Curie temperature for Mn_2TaAl and Mn_2WAl, the Heisenberg exchange coupling parameters are shown in Figure 15, which include the Mn - Mn, Mn-Al and Mn-Ta/W atomic interactions, the other are omitted because of their very small values. Based on the exchange interactions, it is clear the *d-d* (Mn - Mn and Mn-Ta/W) exchange plays an important role in the interactions. Furthermore, all the interactions are limited to the clusters with a radius of $r \leq 2.5$ Å. Next, our focus will be on the details of these exchange interactions.

Initially, let us take the Mn_2TaAl as an example to discuss the interactions, the first nearest-neighbor interaction in the Mn - Mn exchange in the intra-sublattice was found to be positive at about 5 meV, it is negative value for the second nearest neighbor interaction of ∼0.9 meV, the third exchange value ∼1.4 meV is a positive value again, the oscillation behavior shows the RKKY exchange.[78] For the inter-sublattice Mn-Ta exchange, the exchange value is about 1.3 meV. This is because that the Mn atomic moment is larger than that of the Ta or Al atoms. We also find that the first nearest neighbor interaction in the Mn - Mn intra-sublattice is about 2.5 meV, the second nearest neighbor interaction close to zero, and the third exchange value is about 0.6 meV, and the oscillation behavior of the Mn - Mn exchange interactions is obvious, implying an RKKY behavior. The inter-sublattice Mn-W exchange is about 0.7 meV, and other values are close to zero. The Mn - Mn exchange is stronger than the Mn-W/Al exchange because of larger atomic moment. The exchange values for Mn_2TaAl are larger than those of Mn_2WAl, which ascribes to its larger atomic magnetic moment (see Table 3). Finally, it can be concluded that the *d-d* and the RKKY exchange together bring about the occurrence of ferromagnetically ordered phase in both alloys. Based on the above discussion it can be seen that the Mn - Mn exchange contributes significantly to the total exchange. Indeed, positive values of the interaction imply ferromagnetic exchange and negative values imply anti-ferromagnetic exchange. The exchange interactions between constitutions were applied to assess the Curie temperatures of Mn_2TaAl and Mn_2WAl (see Table 3), it can be seen the Curie temperature of Mn_2TaAl is 345.6 K, which is evidently lower than that of Mn_2VAl with 638 K in theory and 760 K in experiment because of smaller Mn - Mn exchange interactions,[79] thus the Mn_2TaAl is likely to be ferrimagnet at room temperature.

Thermodynamic properties

The quasi-harmonic Debye model is used to study the thermodynamic behavior of Mn_2TaAl and Mn_2WAl The Gibbs function $G^*(V;P,T)$ for non-equilibrium state of the system is shown as follows:[80]

$$G^*(V;P,T) = E(V) + PV + A_{Aib}[\Theta(V);T] \quad \text{(Equation 26)}$$

where PV and $E(V)$ are the constant hydrostatic and the total energy, $\Theta(V)$ denotes the Debye temperature, and the A_{Aib} denotes the vibrational term shown as:[81,82]

$$A_{Aib}(\Theta;T) = nk_BT\left[\frac{9}{8}\frac{\Theta}{T} + 3\,ln(1 - e^{-\frac{\Theta}{T}}) - D\left(\frac{\Theta}{T}\right)\right] \quad \text{(Equation 27)}$$

where $\boldsymbol{D}\left(\frac{\Theta}{T}\right)$ is the Debye integral, n is the atomic number per formula unit, k_B and T are the Boltzmann constant and the absolute temperature respectively.

The Θ is expressed as:[81]

$$\Theta = \frac{h}{k_B}\left[6\pi^2V^{\frac{1}{2}}n\right]^{\frac{1}{3}}f(v)\sqrt{\frac{B_s}{M}} \quad \text{(Equation 28)}$$

where M denotes the molar mass, the adiabatic bulk modulus B_s approximates the static compressibility:[80]

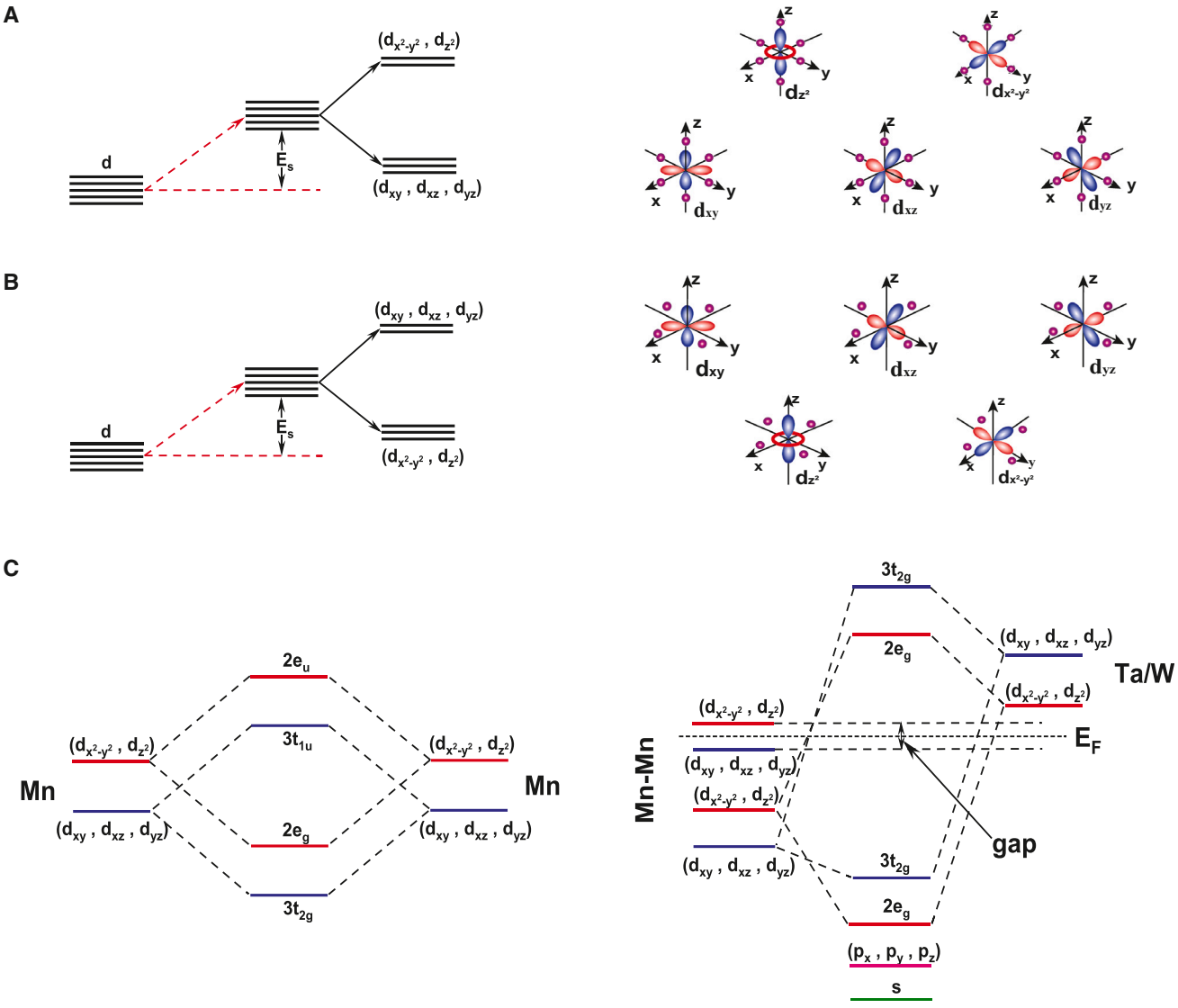

Figure 13. The splitting and occupation of Mn- and Ta/W-*d* orbitals of Mn_2TaAl and Mn_2WAl alloys in the crystal field

$$B_S \cong B_V = V\left(\frac{d^2E(V)}{dV^2}\right) \quad \text{(Equation 29)}$$

$f(v)$ is shown in ref. 82 and. Therefore, the $G^*(V;P,T)$ is minimized to the volume V

$$\left(\frac{\partial G^*(V;P,T)}{\partial V}\right)_{P,T} = 0 \quad \text{(Equation 30)}$$

The isothermal bulk modulus B_T and the heat capacity C_V are shown as follows:[83]

$$B_T(P,T) = V\left(\frac{\partial^2 G^*(V;P,T)}{\partial V^2}\right)_{P,T} \quad \text{Equation (31)}$$

$$C_V = 3nk_B\left[4D\left(\frac{\Theta}{T}\right) - \frac{3\Theta/T}{e^{\frac{\Theta}{T}}-1}\right] \quad \text{(Equation 32)}$$

The Grüneisen parameter γ is usually applied to describe the anharmonic effects of a vibrating lattice and is defined as follows:

$$\gamma = \frac{\partial ln\,\Theta}{\partial lnV} \quad \text{(Equation 33)}$$

$$\alpha = \frac{\gamma C_V}{B_T V} \quad \text{(Equation 34)}$$

where α denotes the coefficient of thermal expansion.

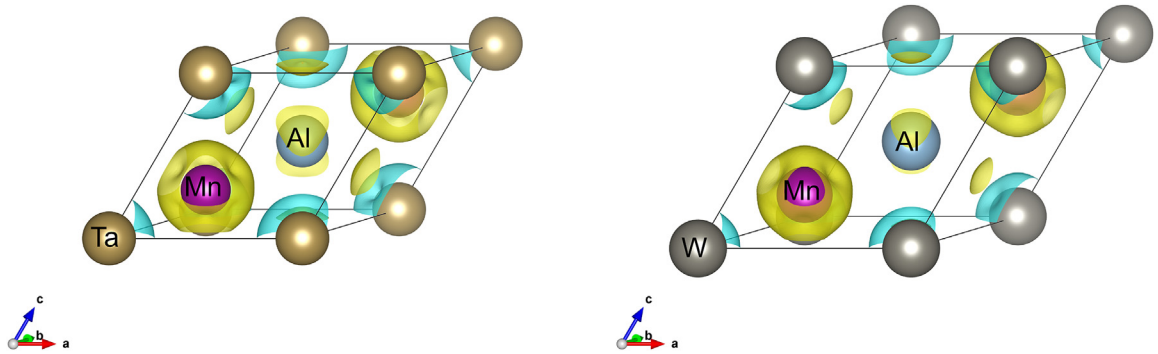

Figure 14. Spin charge density for Mn_2TaAl and Mn_2WAl Heusler alloys

By the model, the thermodynamic characterizations of Mn_2TaAl and Mn_2WAl are determined within 0∼600 K at zero pressure. The changes of $\Theta(V)$, B_s, α and C_V over temperature for Mn_2TaAl and Mn_2WAl are displayed in Figure 16. It is found that the Debye temperature for Mn_2TaAl is about 510 K within room temperature (see Figure 16A), and decrease to ∼490 K with further increasing temperature, the jump of Debye temperature origins from the phase transition from ferrimagnetic to nonmagnetic states. Similarly, for the Mn_2WAl alloy, the Debye temperature is ∼772 K within 113.4 K, and the Debye temperature is about 530 K above the Curie point, the jump is more obvious than Mn_2TaAl. In particular, the variation of Debye temperature over temperature is almost a straight line on both sides of the jump point.

From the Figure 16B, we notice that the B_s of Mn_2TaAl is about 185∼195 GPa below 345.6 K, and increase to about 190 GPa with increasing temperature. However, for the Mn_2WAl, the value of B_s is 469 GPa below 113.4 K, which attains to the 220–230 GPa above 113.4 K, the tendency is similar with the Debye temperature of Mn_2WAl. Likewise, the B_s value with temperature is close to the straight line on both sides of the Curie temperature.

For the thermal expansion α of Mn_2TaAl and Mn_2WAl alloys in Figure 16C, there is a significant jump at the phase transition point, the difference being that the coefficient of thermal expansion decreases for Mn_2TaAl alloys and increases for Mn_2WAl alloys. For the Mn_2TaAl alloy, the coefficient of thermal expansion increases rapidly up to 345.6 K, causing a jump, thereby increases slowly with increasing temperature. As for the Mn_2WAl alloy, it has almost unchanged within 113.4 K, undergoes a jump with further increase in temperature and then increases as the temperature increased. Another aspect, the α of Mn_2TaAl is always higher than that of Mn_2WAl at 0–600 K temperature.

For the Mn_2TaAl alloy, there is a rapid increase within the 200 K as shown in Figure 16D. At temperatures above 200 K, the change in the C_V with temperature tends to a plateau, the change in the C_V on both sides of the phase transition point is not significant, and it is within the range of about 5 J/mol·K. For the Mn_2WAl alloy, the C_V increases over the increasing temperature within 113.4 K, but this increase is obviously slower than that of Mn_2TaAl alloy. Above 113.4 K, the tendency of specific heat capacity of Mn_2WAl alloy is almost the same as that of Mn_2TaAl alloy.

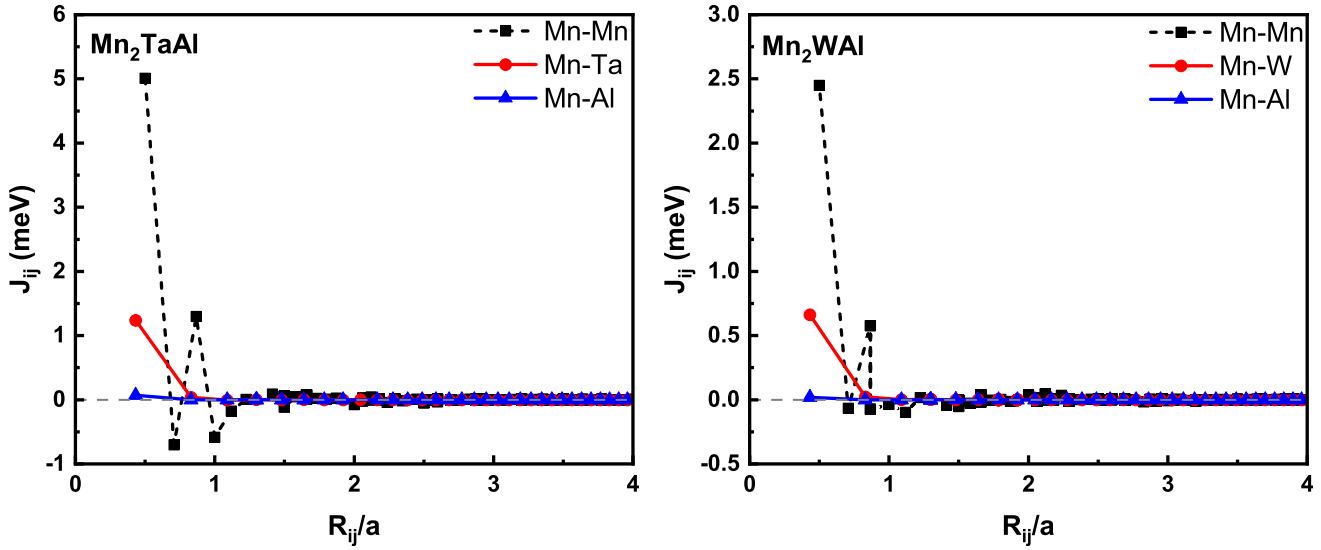

Figure 15. Exchange interactions of Mn_2TaAl and Mn_2WAl alloys with the inter-atomic distance *r*

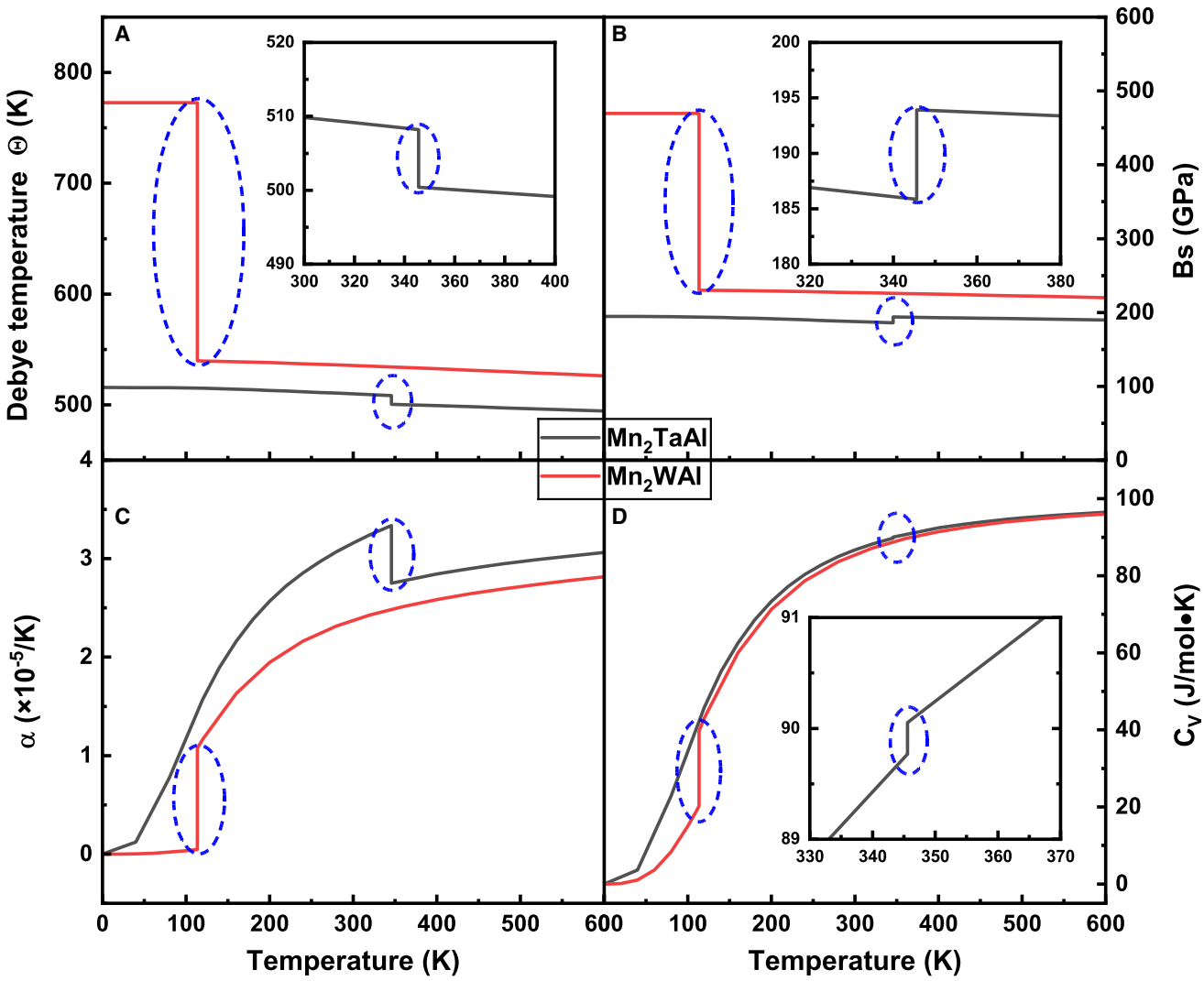

Figure 16. Thermodynamic parameters of Mn_2TaAl and Mn_2WAl alloys

Relationship between (A) Debye temperature Θ, (B) adiabatic bulk modulus B_S, (C) thermal expansion α and (D) specific heat capacity C_V and different temperatures of Mn_2TaAl and Mn_2WAl alloys.

Thermoelectric properties

Finally, we investigated the thermoelectric transport properties of Mn_2TaAl and Mn_2WAl alloys, it should be emphasized that we do not consider the magnetic phase transition in the thermoelectric calculations. In Figure 17, we offer the Seebeck coefficients S, electrical conductivity σ, thermal conductivity κ and thermoelectric merit value zT of Mn_2TaAl and Mn_2WAl alloys within 200∼900 K. First, we calculated the conductivity σ_{tot} as a function of temperature, it is the sum of the spin-up and spin-down conductivities:

$$\sigma_{tot} = \sigma\uparrow + \sigma\downarrow \quad \text{(Equation 35)}$$

We can see from Figure 17 that the conductivity of spin-up electrons increases with temperature, and the conductivity of spin-down electrons decreases almost linearly with temperature, also, total conductivity of two alloys decrease linearly. Second, we calculated the Seebeck coefficient S:

$$S = \frac{S\uparrow\sigma\uparrow + S\downarrow\sigma\downarrow}{\sigma\uparrow + \sigma\downarrow} \quad \text{(Equation 36)}$$

where $S\uparrow(\sigma\uparrow)$ and $S\downarrow(\sigma\downarrow)$ denote the Seebeck coefficients (conductivity) of spin-up and spin-down bands, respectively. For the Mn_2TaAl and Mn_2WAl alloys, the Seebeck coefficient S of spin-down electrons increases with increasing temperature, and the Seebeck coefficients S of spin-up electrons decreases with increasing temperature. The total S of Mn_2TaAl alloy decrease with temperature, and it is slowly increased for Mn_2WAl, which ascribes to the S of spin-up electrons of Mn_2TaAl larger than that of Mn_2WAl. The thermal conductivity

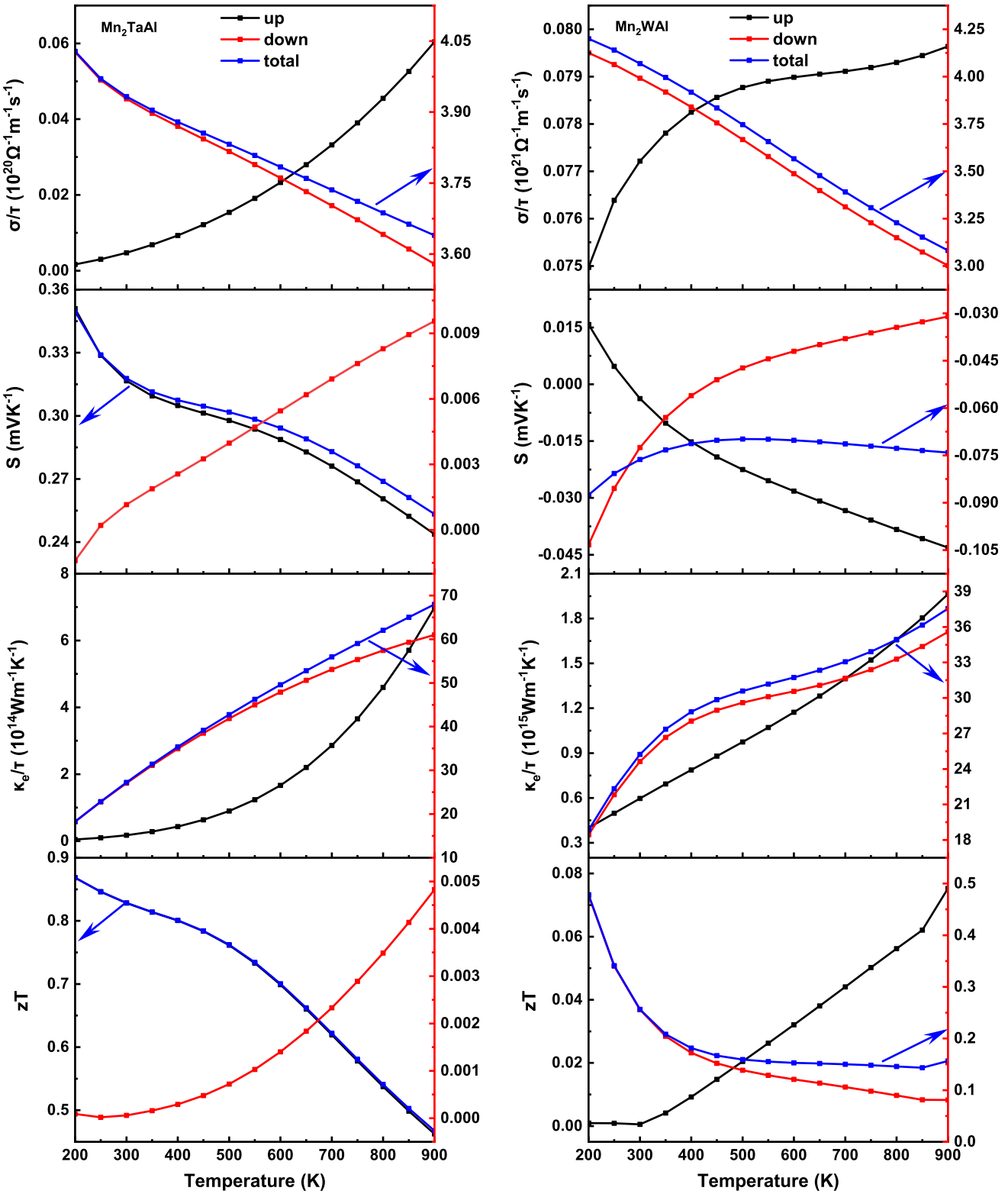

Figure 17. The variation of electrical conductivity (σ/τ), Seebeck coefficient (S), electronic thermal conductivity (κ_e) and thermoelectric merit value (zT) of Mn2TaAl and Mn2WAl alloys with temperature

κ is composed of the electronic thermal conductivity κ_e and the lattice thermal conductivity κ_l, where we only consider the electronic thermal conductivity. The thermal conductivity of both alloys shows the similar tendency, namely, they increase with increasing temperature. Finally, we calculate the zT value of Mn_2TaAl and Mn_2WAl alloys. The zT value is an important parameter for measuring the thermoelectric properties of a material, zT value can be obtained in the following:

$$zT = \frac{S^2\sigma T}{\kappa} \quad \text{(Equation 37)}$$

a larger zT value denotes the higher the conversion efficiency for thermoelectric material. By Equation 37, we obtained the zT value of Mn_2TaAl and Mn_2WAl with temperature, it is found that the largest zT values of Mn_2TaAl and Mn_2WAl are 0.87 at 200 K and 0.48 at 900 K, respectively, thus the Mn_2TaAl can be considered as a better thermoelectric material compared with Mn_2WAl.

Summary and conclusions

Using the first-principles calculations, we have studied the structural stability, Gilbert damping parameter, electronic and magnetic properties, exchange interactions, and Curie temperatures of Mn_2TaAl and Mn_2WAl. Calculations show that two alloys meet the dynamic, mechanical, and thermodynamic stabilities. Phase separation exhibits that Mn_2TaAl and Mn_2WAl are extremely possible to be experimentally synthesized because of their low convex hull. The Gilbert damping for Mn_2TaAl and Mn_2WAl show their fast response speed and lower energy consumption in spintronic applications. The Mn_2TaAl and Mn_2WAl are ferrimagnetic half-metal and nearly half-metal according to the electronic calculations, and their total moments follow $M_t = Z_t - 18$; the exchange splitting of t_{2g} and $e_{.g.,}$ states is mainly responsible for forming the HM gap. The Mn - Mn exchange plays a main role in the interactions, and the competition and collaboration from the *d-d* and RKKY exchanges bring about the ferromagnetically ordered phase. The Curie temperature of Mn_2TaAl is obviously higher apparently than room temperature. Finally, we discuss the changes of Debye temperature, adiabatic bulk modulus, coefficient of thermal expansion and specific heat capacity within 0∼600 K, and Seebeck coefficient, electrical conductivity, thermal conductivity and thermoelectric merit value of both alloys within 200∼900 K. Overall, our calculations might offer some valuable clues for Mn_2TaAl and Mn_2WAl alloys as potential candidates for spintronic devices.

Limitations of the study

For the calculations of thermoelectric properties, we did not consider the lattice thermal conductivity. Also, we did not consider the phase transition at a Curie point.

RESOURCE AVAILABILITY

Lead contact

Further information and requests should be directed to and will be fulfilled by the lead contact, X.-P.W. (weixp2008@lzjtu.edu.cn).

Materials availability

Both materials can be obtained in manuscript.

Data and code availability

- All data will be shared upon request to the lead contact.
- This paper does not report original code.
- Any additional information required to reanalyze the data reported in this work is available from the lead contact upon request.

ACKNOWLEDGMENTS

The work is supported by National Natural Science Foundation of China (No. 12164024 and No. 11864021), the work is also supported by Gansu Longyuan Young Talents Program of China.

AUTHOR CONTRIBUTIONS

Conceptualization, X.P.W. and Y.L.Z; methodology, X.P.W., X.M.T., and J.Y.Z.; software, X.M.T. and J.Y.Z.; formal analysis, X.L. and X.P.W.; data curation, X.L.; writing–original draft, X.L. and X.P.W.; writing–review and editing, X.L. and X.P.W; funding acquisition, X.P.W; supervision, X.P.W., Y.L.Z., and X.M.T.

DECLARATION OF INTERESTS

The authors declare no competing interests.

STAR★METHODS

Detailed methods are provided in the online version of this paper and include the following:

- KEY RESOURCES TABLE
- METHOD DETAILS
- QUANTIFICATION AND STATISTICAL ANALYSIS

Received: August 2, 2024
Revised: September 15, 2024
Accepted: October 23, 2024
Published: October 30, 2024

REFERENCES

1. de Groot, R.A., Mueller, F.M., Engen, P.G.v., and Buschow, K.H.J. (1983). New Class of Materials: Half-Metallic Ferromagnets. Phys. Rev. Lett. *50*, 2024–2027. https://doi.org/10.1103/PhysRevLett.50.2024.
2. Felser, C., Fecher, G.H., and Balke, B. (2007). Spintronics: A Challenge for Materials Science and Solid-State Chemistry. Angew. Chem. Int. Ed. *46*, 668–699. https://doi.org/10.1002/anie.200601815.
3. Graf, T., Felser, C., and Parkin, S.S. (2011). Simple rule for the understanding of Heusler compounds. Prog. Solid State Chem. *39*, 1–50. https://doi.org/10.1016/j.progsolidstchem.2011.02.001.
4. Schwarz, K. (1986). CrO2 predicted as a half-metallic ferromagnet. J. Phys. F: Met. Phys. *16*, L211–L215. https://iopscience.iop.org/article/10.1088/0305-4608/16/9/002/.
5. Dedkov, Y.S., Rüdiger, U., and Güntherodt, G. (2002). Evidence for the half-metallic ferromagnetic state of Fe3O4 by spinresolvedphotoelectron spectroscopy. Phys. Rev. B *65*, 064417. https://doi.org/10.1103/PhysRevB.65.064417.
6. Park, J.-H., Vescovo, E., Kim, H.-J., Kwon, C., Ramesh, R., and Venkatesan, T. (1998). Direct evidence for a half-metallic ferromagnet. Nature *392*, 794–796. https://doi.org/10.1038/33883.
7. Park, J.-H., Vescovo, E., Kim, H.-J., Kwon, C., Ramesh, R., and Venkatesan, T. (1998). Magnetic Properties at Surface Boundary of a Half-Metallic Ferromagnet. Phys. Rev. Lett. *81*, 1953–1956. https://doi.org/10.1103/PhysRevLett.81.1953.

8. Rivero, P., Meunier, V., and Shelton, W. (2017). Half-metallic ferromagnetism in Sr3Ru2O7. Phys. Rev. B *95*, 195106. https://doi.org/10.1103/PhysRevB.95.195106.

9. Xie, W.-H., Xu, Y.-Q., Liu, B.-G., and Pettifor, D.G. (2003). Halfmetallic ferromagnetism and structural stability of zinc blende phases of the transition-metal chalcogenides. Phys. Rev. Lett. *91*, 037204. https://doi.org/10.1103/PhysRevLett.91.037204.

10. Sanyal, B., Bergqvist, L., and Eriksson, O. (2003). Ferromagnetic materials in the zinc-blende structure. Phys. Rev. B *68*, 054417. https://doi.org/10.1103/PhysRevB.68.054417.

11. Karaca, M., Kervan, S., and Kervan, N. (2015). Half-metallic ferromagnetism in the CsSe compound by density functional theory. J. Alloys Compd. *639*, 162–167. https://doi.org/10.1016/j.jallcom.2015.03.164.

12. Liu, B.-G. (2003). Robust half-metallic ferromagnetism in zinc-blende CrSb. Phys. Rev. B *67*, 172411. https://doi.org/10.1103/PhysRevB.67.172411.

13. Li, J., Li, Y., Zhou, G., Sun, Y., and Sun, C.Q. (2009). A first principles study on the full-Heusler compound Cr_2MnAl. Appl. Phys. Lett. *94*, 242502. https://doi.org/10.1063/1.3156811.

14. Wei, X.-P., Deng, J.-B., Mao, G.-Y., Chu, S.-B., and Hu, X.-R. (2012). Half-metallic properties for the Ti2YZ (Y=Fe, Co, Ni, Z=Al, Ga, In) Heusler alloys: A first-principles study. Intermetallics *29*, 86–91. https://doi.org/10.1016/j.intermet.2012.05.002.

15. Wang, X.T., Lin, T.T., Rozale, H., Dai, X.F., and Liu, G.D. (2016). Robust half-metallic properties in inverse Heusler alloys composed of 4d transition metal elements: Zr2RhZ (Z=Al, Ga, In). J. Magn. Magn Mater. *402*, 190–195. https://doi.org/10.1016/j.jmmm.2015.11.062.

16. Deng, Z.-Y., and Zhang, J.-M. (2016). Half-metallic and magnetic properties of full-Heusler alloys Zr2CrZ (Z=Ga, In) with Hg2CuTi-type structure: A first-principles study. J. Magn. Magn Mater. *397*, 120–124. https://doi.org/10.1016/j.jmmm.2015.08.089.

17. Wei, X.-P., Zhang, Y.-L., Wang, T., Sun, X.-W., Song, T., Guo, P., and Deng, J.-B. (2017). Stability, electronic and magnetic properties investigations on Zr2YZ (Y=Co, Cr, V and Z=Al, Ga, In, Pb, Sn, Tl). Mater. Res. Bull. *86*, 139–145. https://doi.org/10.1016/j.materresbull.2016.10.013.

18. Gurunani, B., and Gupta, D.C. (2024). Exploring the multifaceted properties: structural, electronic, magnetic, mechanical, thermodynamic, transport, and optical characteristics of rhodium-based half-Heusler alloys. J. Mater. Sci. *59*, 12502–12525. https://doi.org/10.1007/s10853-024-09942-5.

19. Gurunani, B., and Gupta, D.C. (2023). Exploring the electronic structure, mechanical behaviour, thermal and high-temperature thermoelectric response of CoZrSi and CoZrGe Heusler alloys. Sci. Rep. *13*, 22834. https://doi.org/10.1038/s41598-023-48316-w.

20. Aravindan, V., Rajarajan, A.K., Vijayanarayanan, V., and Mahendran, M. (2022). *Ab initio* study on the CoZrVIn equiatomic quaternary alloy for spintronic and thermoelectric applications. Mater. Today Proc. *65*, 2596–2601. https://doi.org/10.1016/j.matpr.2022.04.872.

21. Farshchi, R., and Ramsteiner, M. (2013). Spin injection from Heusler alloys into semiconductors: A materials perspective. J. Appl. Phys. *113*, 191101. https://doi.org/10.1063/1.4802504.

22. UI, H.S., Khan, I., and Hong, J. (2024). High Curie temperature and high magnetization potential Fe2CoS alloy soft magnet. Phys. Lett. *504*, 129429. https://doi.org/10.1016/j.physleta.2024.129429.

23. Qiao, S., Nie, S., Zhao, J., Huo, Y., Wu, Y., and Zhang, X. (2013). Magnetic and Gilbert damping properties of L21-Co2FeAl filmgrown by molecular beam epitaxy. Appl. Phys. Lett. *103*, 152402. https://doi.org/10.1063/1.4824654.

24. Aravindan, V., Rajarajan, A.K., and Mahendran, M. (2021). First-Principles Study of Structural, Electronic, Magnetic and Elastic Properties of the Mn2XSb (X=Co, Fe) Inverse Heusler Alloys. J. Electron. Mater. *50*, 1786–1793. https://doi.org/10.1007/s11664-020-08688-5.

25. Gurunani, B., and Gupta, D.C. (2023). Tailoring the intrinsic magnetoelectronic, mechanical, thermo-physical and thermoelectric response of cobalt-based Heusler alloys: an *ab initio* insight. RSC Adv. *13*, 29959–29974. https://pubs.rsc.org/en/content/articlehtml/2023/ra/d3ra03957a.

26. Gurunani, B., Ghosh, S., and Gupta, D.C. (2024). Comprehensive investigation of half Heusler alloy: Unveiling structural, electronic, magnetic, mechanical, thermodynamic, and transport properties. Intermetallics *170*, 108311. https://doi.org/10.1016/j.intermet.2024.108311.

27. de Paula, V.G., and Reis, M.S. (2021). All-d-metal full Heusler alloys: A novel class of functional materials. Chem. Mater. *33*, 5483–5495. https://doi.org/10.1021/acs.chemmater.1c01012.

28. Wang, X., Cheng, Z., and Wang, W. (2017). L21 and XA ordering competition in hafnium-based full-heusler alloys Hf2VZ (Z=Al, Ga, In, Tl, Si, Ge, Sn, Pb). Materials *10*, 1200. https://doi.org/10.3390/ma10101200.

29. Salaheldeen, M., Ipatov, M., Corte-Leon, P., Zhukova, V., and Zhukov, A. (2023). Effect of Annealing on the Magnetic Properties of Co2MnSi-Based Heusler Alloy Glass-Coated Microwires. Materials *13*, 412. https://doi.org/10.3390/met13020412.

30. Zhu, X., Jiang, E., Dai, Y., and Luo, C. (2015). Stability, magnetic, and electronic properties of L21 and B2 phases in Co2MnAl Heusler alloy. J. Alloys Compd. *632*, 528–532. https://doi.org/10.1016/j.jallcom.2015.01.198.

31. Abada, A., Amara, K., Hiadsi, S., and Amrani, B. (2015). First principles study of a new half-metallic ferrimagnets Mn2-based full Heusler compounds: Mn2ZrSi and Mn_2ZrGe. J. Magn. Magn Mater. *388*, 59–67. https://doi.org/10.1016/j.jmmm.2015.04.023.

32. Umetsu, R.Y., Morimoto, N., Nagasako, M., Kainuma, R., and Kanomata, T. (2012). Annealing temperature dependence of crystal structures and magnetic properties of Fe2CrAl and Fe2CrGa Heusler alloys. J. Alloys Compd. *528*, 34–39. https://doi.org/10.1016/j.jallcom.2012.02.163.

33. Yin, M., Nash, P., Chen, W., and Chen, S. (2016). Standard enthalpies of formation of selected Ni_2YZ Heusler compounds. J. Alloys Compd. *660*, 258–265. https://doi.org/10.1016/j.jallcom.2015.11.126.

34. Itoh, H., Nakamichi, T., Yamaguchi, Y., and Kazama, N. (1983). Neutron diffraction study of Heusler type alloy Mn0.47V0.28Al0.25. J. Jpn. Inst. Met. *24*, 265–271. https://doi.org/10.2320/matertrans1960.24.265.

35. Buffat, P., and Borel, J.-P. (1976). Size effect on the melting temperature of gold particles. Phys. Rev. A *13*, 2287–2298. https://doi.org/10.1103/PhysRevA.13.2287.

36. Weht, R., and Pickett, W.E. (1999). Half-metallic ferrimagnetism in Mn2VAl. Phys. Rev. B *60*, 13006–13010. https://doi.org/10.1103/PhysRevB.60.13006.

37. Jiang, C., Venkatesan, M., and Coey, J.M.D. (2001). Transport and magnetic properties of Mn_2VAl: Search for half-metallicity. Solid State Commun. *118*, 513–516. https://doi.org/10.1016/S0038-1098(01)00151-X.

38. Koepernik, K., and Eschrig, H. (1999). Full-potential nonorthogonal local-orbital minimum-basis band-structure scheme. Phys. Rev. B *59*, 1743–1757. https://doi.org/10.1103/PhysRevB.59.1743.

39. Eschrig, H., Richter, M., and Opahle, I. (2004). Relativistic solid state calculations. Comput. Theor. Chem. *14*, 723–776. https://doi.org/10.1016/S1380-7323(04)80039-6.

40. Kresse, G., and Furthmüller, J. (1996). Efficiency of *ab-initio* total energy calculations for metals and semiconductors using a plane-wave basis set. Comput. Mater. Sci. *6*, 15–50. https://doi.org/10.1016/0927-0256(96)00008-0.

41. Kresse, G., and Joubert, D. (1999). From ultrasoft pseudopotentials to the projector augmented-wave method. Phys. Rev. B *59*, 1758–1775. https://doi.org/10.1103/PhysRevB.59.1758.

42. Monkhorst, H.J., and Pack, J.D. (1976). Special points for Brillouin-zone integrations. Phys. Rev. B *13*, 5188–5192. https://doi.org/10.1103/PhysRevB.13.5188.

43. Ebert, H., Ködderitzsch, D., and Minár, J. (2011). Calculating condensed matter properties using the KKR-Green's function methorecent

developments and applications. Rep. Prog. Phys. *74*, 096501. https://iopscience.iop.org/article/10.1088/0034-4885/74/9/096501/meta.

44. Lloyd, P., and Smith, P.V. (1972). Multiple scattering theory in condensed materials. Adv. Phys. X. *21*, 69–142. https://doi.org/10.1080/00018737200101268.

45. Zeller, R. (2008). Improving the charge density normalization in Korringa-Kohn-Rostoker Green-function calculations. J. Phys-condens Mat. *20*, 035220. https://iopscience.iop.org/article/10.1088/0953-8984/20/03/035220/meta.

46. Vosko, S.H., Wilk, L., and Nusair, M. (1980). Accurate spin-dependent electron liquid correlation energies for local spin density calculations: a critical analysis. Can. J. Phys. *58*, 1200–1211. https://doi.org/10.1139/p80-159.

47. Zagrebin, M.A., Matyunina, M.V., Sokolovskiy, V.V., and Buchelnikov, V.D. (2019). The effect of exchange-correlation potentials on magnetic properties of Fe-(Ga, Ge, Al) alloys. J. Phys, Conf. Ser. *1389*, 012087. https://iopscience.iop.org/article/10.1088/17426596/1389/1/012087/meta.

48. Liechtenstein, A.I., Katsnelson, M.I., Antropov, V.P., and Gubanov, V.A. (1987). Local spin density functional approach to the theory of exchange interactions in ferromagnetic metals and alloys. J. Magn. Magn Mater. *67*, 65–74. https://doi.org/10.1016/0304-8853(87)90721-9.

49. Liechtenstein, A.I., Katsnelson, M.I., and Gubanov, V.A. (1984). Exchange interactions and spin-wave stiffness in ferromagnetic metals. J. Phys. F: Met. Phys. *14*, L125–L128. https://iopscience.iop.org/article/10.1088/0305-4608/14/7/007/meta.

50. Katsnelson, M.I., and Lichtenstein, A.I. (2000). First-principles calculations of magnetic interactions in correlated systems. Phys. Rev. B *61*, 8906–8912. https://doi.org/10.1103/PhysRevB.61.8906.

51. Wei, X.-P., Zhang, Y.-L., Sun, X.-W., Song, T., Guo, P., Gao, Y., Zhang, J.L., Zhu, X.F., and Deng, J.B. (2017). Exchange interactions and Curie temperatures in Fe_2NiZ compounds. J. Alloys Compd. *694*, 1254–1259. https://doi.org/10.1016/j.jallcom.2016.10.105.

52. Wei, X.P., and Zhou, Y.H. (2018). First-principles and Monte Carlo studies of the Fe2NiZ compounds on exchange interactions and Curie temperatures. Intermetallics *93*, 283–289. https://doi.org/10.1016/j.intermet.2017.10.006.

53. Wei, X.P., Gao, P., Zhang, Y.L., and Zhang, H. (2019). Investigations on exchange interactions and Curie temperatures of Zr2CoZ compounds by using first-principles and Monte Carlo calculations. J. Magn. Magn Mater. *477*, 190–197. https://doi.org/10.1016/j.jmmm.2019.01.051.

54. Wang, L., Ding, B., and Guo, Y. (2019). Spin-polarized transport behavior induced by asymmetric edge hydrogenation in hybridized zigzag boron nitride and graphene nanoribbons. J. Electron. Mater. *48*, 321–328. https://doi.org/10.1007/s11664-018-6711-x.

55. Raïâ, M.Y., Masrour, R., Hamedoun, M., Kharbach, J., Rezzouk, A., Hourmatallah, A., Benzakour, N., and Bouslykhane, K. (2022). Stability, magnetic, electronic, elastic, thermodynamic, optical and thermoelectric properties of Co2TiSn, Co2ZrSn and Co2HfSn Heusler alloys from calculations using generalized gradient approximation techniques. J. Mater. Sci. *33*, 20229. https://doi.org/10.1007/s10854-022-08841-2.

56. Kirklin, S., Saal, J.E., Meredig, B., Thompson, A., Doak, J.W., Aykol, M., Rühl, S., and Wolverton, C. (2015). The Open Quantum Materials Database (OQMD): assessing the accuracy of DFT formation energies. npj Comput. Mater. *1*, 15010. https://doi.org/10.1038/npjcompumats.2015.10.

57. Gao, Q., Opahle, I., and Zhang, H. (2019). High-throughput screening for spin-gapless semiconductors in quaternary Heusler compounds. Phys. Rev. Mater. *3*, 024410. https://doi.org/10.1103/PhysRevMaterials.3.024410.

58. Chang, Y., Chen, S., Zhang, F., Yan, X., Xie, F., SchmidFetzer, R., and Oates, W. (2004). Phase diagram calculation: past, present and future. Prog. Mater. Sci. *49*, 313–345. https://doi.org/10.1016/S0079-6425(03)00025-2.

59. Hill, R. (1952). The elastic behaviour of a crystalline aggregate. Proc. Phys. Soc. *65*, 349–354. https://iopscience.iop.org/article/10.1088/0370-1298/65/5/307/meta.

60. Chung, D.H., and Buessem, W.R. (1967). The voigt-reuss-hill approximation and elastic moduli of polycrystalline MgO, CaF2, ZnSe, and CdTe. J. Appl. Phys. *38*, 2535–2540. https://doi.org/10.1063/1.1709944.

61. Saha, S.K., and Dutta, G. (2016). Elastic and thermal properties of the layered thermoelectrics BiOCuSe and LaOCuSe. Phys. Rev. B *94*, 125209. https://doi.org/10.1103/PhysRevB.94.125209.

62. Yousuf, S., and Gupta, D.C. (2018). Insight into half-metallicity, spin polarization and mechanical properties of L21 structured MnY_2Z (Z=Al, Si, Ga, Ge, Sn, Sb) Heusler alloys. J. Alloys Compd. *735*, 1245–1252. https://doi.org/10.1016/j.jallcom.2017.11.239.

63. I, J. Solid state physics simulations. 1996.

64. Benkabou, M., Rached, H., Abdellaoui, A., Rached, D., Khenata, R., Elahmar, M.H., Abidri, B., Benkhettou, N., and Bin-Omran, S. (2015). Electronic structure and magnetic properties of quaternary Heusler alloys CoRhMnZ (Z=Al, Ga, Ge and Si) via first-principle calculations. J. Alloys Compd. *647*, 276–286. https://doi.org/10.1016/j.jallcom.2015.05.273.

65. Wei, X.-P., Zhang, X., Shen, J., Chang, W.-L., and Tao, X. (2022). Gilbert damping, electronic and magnetic properties for quaternary Heusler alloys CrYCoZ: First-principles and Monte Carlo studies. Comput. Mater. Sci. *210*, 111453. https://doi.org/10.1016/j.commatsci.2022.111453.

66. Li, T., Zhou, D.W., Yan, Y.R.L., Peng, P., and Liu, J.-S. (2021). First-principles and experimental investigations on ductility/brittleness of intermetallic compounds and joint properties in steel/aluminum laser welding. T. Nonferr. Metal Soc. *31*, 2962–2977. https://doi.org/10.1016/S1003-6326(21)65706-0.

67. Green, D.J. (1998). An introduction to the mechanical properties of ceramics (Cambridge University Press).

68. Ebert, H., Mankovsky, S., Ködderitzsch, D., and Kelly, P.J. (2011). *Ab-initio* calculation of the gilbert damping parameter via the linear response formalism. Phys. Rev. Lett. *107*, 066603. https://doi.org/10.1103/PhysRevLett.107.066603.

69. Mankovsky, S., Ködderitzsch, D., Woltersdorf, G., and Ebert, H. (2013). First-principles calculation of the gilbert damping parameter via the linear response formalism with application to magnetic transition metals and alloys. Phys. Rev. B *87*, 014430. https://doi.org/10.1103/PhysRevB.87.014430.

70. Ebert, H., and Mankovsky, S. (2009). Anisotropic exchange coupling in diluted magnetic semiconductors: Ab initio spin-density functional theory. Phys. Rev. B *79*, 045209. https://doi.org/10.1103/PhysRevB.79.045209.

71. Butler, W.H. (1985). Theory of electronic transport in random alloys: Korringa-kohn-rostoker coherent-potential approximation. Phys. Rev. B *31*, 3260–3277. https://doi.org/10.1103/PhysRevB.31.3260.

72. Jürgen, H., and Jaffe, H.H. (1963). Slater-Condon Parameters from Spectral Data. J. Chem. Phys. *38*, 1834. https://doi.org/10.1063/1.1733882.

73. Mavropoulos, P., Galanakis, I., Popescu, V., and Dederichs, P.H. (2004). The influence of spin–orbit coupling on the band gap of Heusler alloys. J. Phys. Condens. Matter *16*, S5759–S5762. https://iopscience.iop.org/article/10.1088/0953-8984/16/48/043/meta.

74. Becke, A.D., and Edgecombe, K.E. (1990). A simple measure of electron localization in atomic and molecular systems. J. Chem. Phys. *92*, 5397–5403. https://doi.org/10.1063/1.458517.

75. Wei, X.-P., Mei, Z.-Y., Liu, X., and Tao, X. (2024). Investigations on stability, Gilbert damping, electronic and magnetic properties along with Curie temperature for quaternary Heusler alloys CrTiCoZ. Results Phys. *58*, 107512. https://doi.org/10.1016/j.rinp.2024.107512.

76. Skaftouros, S., Özdoğan, K., Şaşıoğlu, E., and Galanakis, I. (2013). Generalized Slater-Pauling rule for the inverse Heusler compounds. Phys. Rev. B *87*, 024420. https://doi.org/10.1103/PhysRevB.87.024420.

77. Özdogan, K., Şaşıoğlu, E., and Galanakis, I. (2013). Slater-Pauling behavior in LiMgPdSn-type multifunctional quaternary Heusler materials: Half-metallicity, spin-gapless and magnetic semiconductors. J. Appl. Phys. *113*, 193903. https://doi.org/10.1063/1.4805063.

78. Şaşioğlu, E., Sandratskii, L.M., Bruno, P., and Galanakis, I. (2005). Exchange interactions and temperature dependence of magnetization in half-metallic Heusler alloys. Phys. Rev. B *72*, 184415. https://doi.org/10.1103/PhysRevB.72.184415.

79. Şaşioğlu, E., Sandratskii, L.M., and Bruno, P. (2005). First-principles study of exchange interactions and Curie temperatures of half-metallic ferrimagnetic full Heusler alloys Mn2VZ (Z=Al, Ge). J. Phys. Condens. Matter *17*, 995. https://iopscience.iop.org/article/10.1088/0953-8984/17/6/017/meta.

80. Blanco, M.A., Francisco, E., and Luaña, V. (2004). GIBBS: isothermal-isobaric thermodynamics of solids from energy curves using a quasi-harmonic Debye model. Comput. Phys. Commun. *158*, 57–72. https://doi.org/10.1016/j.comphy.2003.12.001.

81. Blanco, M.A., Pendás, A.M., Francisco, E., Recio, J.M., and Franco, R. (1996). Thermodynamical properties of solids from microscopic theory: applications to MgF2 and Al2O3. J. Mol. Struct. Theochem *368*, 245. https://doi.org/10.1016/S0166-1280(96)90571-0.

82. Flórez, M., Recio, J.M., Francisco, E., Blanco, M.A., and Pendás, A.M. (2002). First-principles study of the rocksalt–cesium chloride relative phase stability in alkali halides. Phys. Rev. B *66*, 144112. https://doi.org/10.1103/PhysRevB.66.144112.

83. Francisco, E., Blanco, M.A., and Sanjurjo, G. (2001). Atomistic simulation of SrF2 polymorphs. Phys. Rev. B *63*, 094107. https://doi.org/10.1103/PhysRevB.63.094107.

STAR★METHODS

KEY RESOURCES TABLE

REAGENT or RESOURCE	SOURCE	IDENTIFIER
Software and algorithms		
Vienna ab initio simulation package	Kresse et al.[40]	https://www.vasp.at/
SPRKKR	Ebert et al.[43]	https://www.ebert.cup.unimuenchen.de/old/index.php?option=com_content&view=article&id=8%3Asprkkr&catid=4%3Asoftware&Itemid=7&lang=en
FPLO	Koepernik et al.[38]	FPLO – a full-potential local-orbital minimum-basis code

METHOD DETAILS

The detailed numerical setting in first-principles calculations have been presented in **Calculation details**.

QUANTIFICATION AND STATISTICAL ANALYSIS

Our study does not include statistical analysis or quantification.